

DEEP SURFACE BRIGHTNESS PROFILES OF SPIRAL GALAXIES FROM SDSS STRIPE82: TOUCHING STELLAR HALOS

JUDIT BAKOS & IGNACIO TRUJILLO

Instituto de Astrofísica de Canarias, C/ Vía Lactea S/N, La Laguna, Tenerife, Spain and
 Departamento de Astrofísica, Universidad de La Laguna, E-38205, La Laguna, Tenerife, Spain

Draft version March 2, 2013

ABSTRACT

Using SDSS *Stripe82* data we have obtained deep radial surface brightness profiles of 7 face-on to intermediate inclined late-type spirals down to $\mu_{r'} \sim 30$ mag arcsec⁻². We do not find any evidence for a sharp cut-off of the light distribution of the disks but a smooth continuation into the stellar halos of galaxies. Stellar halos start to affect the surface brightness profiles of the galaxies at $\mu_{r'} \sim 28$ mag arcsec⁻², and at a radial distance of $\gtrsim 4 - 10$ inner scale-lengths. We find that the light contribution from the stellar halo could be responsible of previous classification of surface brightness profiles as Type III in late-type galaxies. In order to estimate the contribution of the stellar halo light to the total galaxy light, we carried out a Bulge/Disk/Stellar Halo decomposition by simultaneously fitting all components. The light contribution of the halo to the total galaxy light varies from $\sim 1\%$ to $\sim 5\%$, but in case of ongoing mergers, the halo light fraction can be as high as $\sim 10\%$, independently of the luminosities of the galaxies. We have also explored the integrated $(g' - r')$ color of the stellar halo of our galaxies. We find $(g' - r')$ colors ranging from ~ 0.4 to ~ 1.2 . By confronting these colors with model predictions, we encounter problems to fit our very red colors onto stellar population grids with conventional IMFs. Very red halo colors can be attributed to stellar populations dominated by very low mass stars of low to intermediate metallicity produced by bottom-heavy IMFs.

Subject headings: Galaxies: Evolution, Galaxies: Formation, Galaxies: Spiral, Galaxies: Structure
 Galaxies: Photometry, Galaxies: Stellar Halos

1. INTRODUCTION

The faint outer disk and stellar halo of spiral galaxies hold a plethora of information related to their formation and evolution. This is because, due to their relatively long star formation and dynamical time-scales, the fossil records left behind by the formation processes survive longer than in the inner parts of the galaxies. Consequently, the characteristics of these faint subcomponents must be closely connected to the evolutionary paths the galaxies might have taken. Studying the structure and stellar populations of the faint outer disks and stellar halos makes possible to test the predictions of the current cosmological paradigm in detail.

The disks of spiral galaxies have been studied in great detail. Structural studies of nearby spiral galaxies often concern the inner, bright structure, the bulge, bar(s), rings, etc (e.g. de Jong 1996; Graham 2001; MacArthur et al. 2003). During the past decade, however, our knowledge of the structure and stellar populations of the disks at faint surface brightness levels has grown abundantly. These studies pushed the surface brightness limit to $\mu_{r'} \sim 27$ mag arcsec⁻² being able to explore the faint outskirts of disks. Thanks to these efforts, not only we got to know that a large amount of stars is present (Pohlen et al. 2002; Erwin et al. 2005; Pohlen & Trujillo 2006, PT06 hereafter; Erwin et al. 2008) in these regions where star formation is negligible, but they also showed that the paradigm of 'disk-as-exponential' (Patterson 1940; de Vaucouleurs 1958; Freeman 1970) is far from accurate.

Based on their behavior galaxy surface brightness profiles are classified into three major classes termed as Type I, Type II, and Type III. Type I galaxies follow pure exponential profiles. The Type II morphology represents all galaxies with a "downbending break": a double exponential profile with a steeper outer exponential (Pohlen et al. 2002; PT06; Erwin et al. 2008). This class is the revisited and extended version of the Freeman Type II class (Freeman 1970) now including the so-called truncations discovered by van der Kruit (1979). Type III galaxies show an "upbending break", a double exponential profile with a less inclined outer exponential discovered by Erwin et al. (2005). PT06 showed that only a minority of the surface brightness profiles of late-type disks follow a single exponential decline. The majority of late-type disks, $\sim 90\%$, exhibits so called breaks in the faint outer regions. Apart from the fact that these features can be linked to different morphological features (such as bars, rings, spiral arms, etc) inside the disk, the properties of breaks follow tight correlations with the host galaxy properties, like Hubble-type, total luminosity or stellar mass, and disk scale-length. Type II phenomenon is not limited to the local universe, but has also been found in galaxies at higher redshift (Pérez 2004; Trujillo & Pohlen 2005). Moreover, Azzollini et al. (2008b) showed that the break radius could be used as a tracer of size evolution of disk galaxies. In the last ~ 8 Gyrs, Type II disks went through significant (size) evolution.

The stellar population properties obtained via color profiles revealed further clues and can be used to constrain models (Roškar et al. 2008;

Sánchez-Blázquez et al. 2009; Martínez-Serrano et al. 2009) that besides the effect of the motion of the stars (e.g. radial migration) consider the effects of star formation, and/or the threshold in star formation (Kennicutt 1989). Bakos et al. (2008) showed that these three surface brightness types directly translate into distinct behavior on their (g'-r') color profiles. In Type II galaxies the color profile follows a prominent “U-shape”, with the bluest color at the break radius. This suggests that in Type II galaxies the origin of the break phenomena is related to star formation thresholds (e.g. Schaye 2004). By having extended the analysis to intermediate redshifts, it is seen that the “U-shape” of the (g'-r') color profiles is present in the last ~ 8 Gyrs (Azzollini et al. 2008a), revealing that not just the morphology but the *distribution of stellar population content* is a common feature during the evolution of Type II galaxies.

The surface brightness levels that are required to explore the distribution of stars inside the disks are relatively bright ($\mu_{r'} \lesssim 27$ mag arcsec $^{-2}$), making it possible to carry out photometric studies of disks to large distances (even to intermediate redshifts) on statistically representative samples. The stellar halos of spiral galaxies are, however, so faint that to observe them it is necessary to go ~ 10 magnitudes below the night sky level (to reach ~ 30 mag arcsec $^{-2}$). This requires nothing less but excellent observing conditions free of observational artifacts such as flat-fielding problems or large skysubtraction uncertainties. Hitherto only a few *integrated* photometric studies can be found in the literature that have attempted to reach the surface brightness of stellar halos (e.g. Zibetti et al. 2004; Jablonka et al. 2010, and references therein). To investigate the statistical properties of stellar halos Zibetti & Ferguson (2004) and Bergvall et al. (2010) stacked ~ 1000 galaxies arriving at the level of $\mu_{r'} \sim 31$ mag arcsec $^{-2}$. These observations have also revealed anomalous red colors in stellar halos (otherwise known as the “red halo phenomenon”) that could indicate the presence of extreme stellar populations (see also e.g. Lequeux et al. 1998; Zibetti & Ferguson 2004; Zackrisson et al. 2006, 2012).

Another way to explore the stellar population properties of stellar halos is achieved by ‘resolved star’ technique. By probing, for instance, RGB stars inside the stellar halos (e.g. Ferguson et al. 2002; Davidge 2003; Ferguson et al. 2007; Rejkuba et al. 2009; Barker et al. 2012, and references therein), this method proved to be efficient in reaching surface brightness levels that are $\gtrsim 2$ magnitude deeper than what was so far accomplished by integrated photometry. However, the number of systems that can be studied by this technique is largely limited by the resolving power of current telescopes that only allows us to resolve stars in galaxies in our close vicinity (~ 15 Mpc). Despite of this, these studies provided stellar population and spatial constraints of stellar halos with unprecedented certainty. With the current cosmological paradigm in accordance, there is a growing consensus that the stellar halos of nearby galaxies such as M31, NGC 2403, NGC 0891 or M81 are dominated by old but metal-poor populations. There is also compelling evidence that stellar halos are full of tidal debris, remnants of recent mergers

with satellites of these giant galaxies. One of the most well studied galaxies, our neighbor, M31 went through quite a exciting merger history and hence is full of substructures (e.g. Ferguson et al. 2002; Ibata et al. 2007; McConnachie et al. 2009; Tanaka et al. 2010), similarly to the stellar halo of the Milky Way (e.g. Ibata et al. 1994; Majewski et al. 1999; Newberg et al. 2002; Gilmore et al. 2002; Belokurov et al. 2007; Jurić et al. 2008; Bell et al. 2008). There is also plenty of observational evidence showing ongoing merger phenomenology in spiral galaxies at these surface brightness levels, stellar streams have been detected around disk galaxies like NGC 5907, NGC 4013 (Martínez-Delgado et al. 2008, 2009) and NGC 0891 (Mouhcine et al. 2010).

One of the expectations of the current cosmological paradigm is that properties of the stellar halo (e.g. metallicity) correlates with the properties of the host galaxy (e.g. Brook et al. 2004; Bullock & Johnston 2005; Cooper et al. 2010). Although, these correlations might be obscured due to stochastic variations in the merger/accretion history. Disks are expected to be less changed by external phenomena but more driven by *secular* processes. To be able to distinguish between the consequences of these two entirely different effects, and to be able to discern the dominant mechanisms that shape spiral galaxies, we need to study the disks and stellar halos simultaneously in as many systems as possible by reaching low surface brightness levels.

The aim of this paper is to study the structure and stellar content of 7 late-type, intermediate inclined to face-on spiral galaxies down to a surface brightness level of $\mu_{r'} \sim 30$ mag arcsec $^{-2}$ using *integrated light* photometry that beforehand could only be reached by resolved star technique on individual galaxies. With this work we would like to demonstrate that with a *correct data reduction* it is possible to study faint systems like the stellar halo around external galaxies as far as ~ 100 Mpc using the *Stripe82* dataset. This opens the possibility to explore a large variety of galaxy types and masses that are not present in our vicinity.

2. THE SAMPLE

We have created a sample of late-type spiral galaxies selected from the Hyperleda¹ online catalog applying several criteria for the Hubble-type (T parameter), the axis ratio (major axis/minor axis), the absolute B-magnitude (M_{abs}), and the radial velocity relative to the Local Group (corrected for virgocentric inflow, v_{vir}).

We restricted the Hubble-type to cover the types between Sbc and Sdm ($2.99 < T < 8.49$), building up an intermediate- to late-type sample. The axis ratio is selected to be $\log r_{25} < 0.301$ (corresponding to an inclination of $\leq 61^\circ$). This allows us to have a face-on to intermediate inclined galaxy sample, and to mitigate problems related to dust extinction. The distance of our galaxies was restricted accordingly to create a volume-limited but complete sample of galaxies with $M_{abs} < -18.4$ B-mag (see PT06). To this end, we selected galaxies that conform a radial velocity (corrected for the Virgo infall) $v_{vir} < 3250$ km sec $^{-1}$ (out to ~ 46 Mpc estimated following the Hubble relation with $H_0 = 70$ km s $^{-1}$ Mpc $^{-1}$). Hyperleda yields a sample ~ 800 galaxies with

¹ <http://leda.univ-lyon1.fr/>

Table 1
The Sample

Galaxy	α	δ	Hubble	T	D	M_{abs}
(1)	(2)	(3)	type	(5)	[Mpc]	[B-mag]
			(4)		(6)	(7)
NGC0450	01 15 30.4	-00 51 40	SABc	5.8 ± 0.5	24.4	-19.78
NGC0941	02 28 27.8	-01 09 06	SABc	5.3 ± 0.7	21.9	-19.13
NGC1068	02 42 40.7	-00 00 48	Sb	3.0 ± 0.3	15.3	-21.50
NGC1087	02 46 25.1	-00 29 55	SABc	5.2 ± 0.8	20.7	-20.65
NGC7716	23 36 31.4	+00 17 50	SBb	3 ± 0.5	36.5	-20.31
UGC02081	02 36 00.9	+00 25 13	SABc	5.8 ± 0.5	36.5	-18.53
UGC02311	02 49 27.9	-00 52 23	SBb	3.0 ± 0.4	102.8	-21.50

no coordinate restrictions applied. To identify the galaxies that fall within the area (~ 270 square-degrees) of *Stripe82*, we carried out a cross correlation between the full Hyperleda sample and the *Stripe82* catalog. We also added a luminosity extended sample into this cross correlation, containing late-type spirals brighter than $M_{abs} < -20.5$ B-mag by allowing $v_{vir} < 7000$ km sec $^{-1}$.

In total in this paper we explored the following 7 spiral galaxies: NGC 0450, NGC 0941, NGC 1068, NGC 1087, NGC 7716, UGC 02081, and UGC 02311. The sample properties can be found in Table 1.

3. DATA AND PROFILE EXTRACTION

3.1. The Data

Our imaging data come from the Sloan Digital Sky Survey *Stripe82*. This stripe covers about ~ 270 square degrees of the sky in the equatorial plane and has been observed in all SDSS bands multiple, often more than 80, times as part of the SDSS Supernovae Legacy Survey (Abazajian et al. 2009). Even though this particular survey was carried out to study variable objects, this implies that after stacking the data is ~ 2 magnitudes deeper than the regular SDSS imaging. This makes *Stripe82* presently the largest deep sky survey in the optical regime.

3.2. *Stripe82* Stacking

The SDSS archive provides coadded imaging of *Stripe82*, but only of the first season of observations (the SDSS *Stripe82* coaddition is explained in Annis et al. 2011). We carried out different testing on these coadds. By having obtained surface brightness profiles of our galaxies from these images, it became evident that their coaddition process did not provide imaging with sufficient quality for our purposes. For this reason, we developed our own pipeline to carry out (1) the sky subtraction on the downloaded chips; (2) the quality check of all the available runs; and (3) statistical rejection of low quality runs and the stacking. The pipeline is fully automatic and is mostly written in IDL, but makes use of a few external programs, as well.

All the SDSS observations can be downloaded from the SDSS Data Archive Server (SDSS DAS). Before downloading any image from DAS, we need to decide the size of the stack mosaic that include enough area to extract the surface brightness profiles of our galaxies and estimate any residual sky affecting those. A field-of-view (FOV) of ~ 10 times the D_{25} proved to be sufficiently large to carry out the profile extraction. To download the

images, we extract several information from CasJobs². SDSS images are identified by their *run*, *rerun*, *camcol*, and *field* numbers. Casjobs returns these numbers corresponding to the position of our target galaxies within a given search radius. (The search radius due to simple geometry is $\sim \sqrt{2} \times \text{FOV}/2$) The downloaded *Stripe82* chips are flatfielded and bias-free, but they lack calibration and still contain background. In our pipeline we did not include any calibration process, since what we need is a sufficient number of good quality imaging. We further explain the photometric calibration of the final stacks in Section 3.3.

After removing the 1000 counts of the SOFTBIAS added to all SDSS chips, the skyvalue is estimated in the following way. We measure the fluxes in about ten thousand randomly placed, 5 pixel wide apertures. We apply a resistant mean to the distribution of the aperture fluxes, and carry out several iterations to get rid of the fluxes biased by stars, and other background objects. The mean of the bias-free distribution provides accurate measurement of the sky background, and is then subtracted from the chips. The skylevel and the background scatter also serve as parameters to take into account when assessing the quality of the imaging run.

After obtaining the mean sky value and scatter of all runs, we study the distribution of these values. To avoid stacking runs with high background, for instance runs observed around full moon, we reject runs where the skylevel is a 3-sigma outlier from the robust mean of all runs. We also need to be careful about not to stack chips with relevant sky gradient, or chips which show signs of detector degradation. To assess skygradients and possible chip anomalies, we use the same scatter information. In case of flat background the skylevel-skysigma relation is expected to conform the same relation for all the runs. For this reason, we fit this skylevel-skysigma relation and reject runs where it lies beyond 1-sigma error of the expected scatter value.

We also would have liked to avoid problems caused by wide-spread PSFs on our final stacks, to this end we only stacked runs with $\text{FWHM} \leq 1.7$ arcseconds. To this end, we measured the seeing on every run. We used a program called PSFEX (Bertin 2010a) to extract the FWHM. This program makes a robust fit of the PSF by using the stars extracted by SExtractor (Bertin & Arnouts 1996). It is also important to avoid stacking of imaging with high extinction. Since *Stripe82* observations do not come with photometric calibration, we needed to estimate the

² <http://casjobs.sdss.org/CasJobs/>

Table 2
Stack and profile quality

Galaxy	r'-band layers	T_{exp} (min)	$\mu_{3\sigma}$	$\mu_{\pm\sigma-limit}$
NGC0450	(31)42	~ 38	29.5	28.8
NGC0941	47	~ 42	29.9	29.4
NGC1068	60	~ 54	30.1	29.5
NGC1087	55	~ 45	29.0	28.6
NGC7716	(38)58	~ 52	29.4	28.9
UGC02081	(43)53	~ 48	29.8	29.2
UGC02311	66	~ 60	29.4	28.9

level of atmospheric extinction in a crude way. We extracted stars from every run, and measured the fluxes in an aperture both on the *Stripe82* run and on the DR7 image. The mean ratio of the measurements computed for all stars in the run was used as a first-order estimate of the extinction: we rejected a particular run, if we found more than 15% difference of the measured fluxes compared to DR7. Based their histogram, we found that the majority of the runs ($\gtrsim 60\%$) is within this flux difference from DR7, hence this enabled us to create stacks using most of the observations.

Since there have been *Stripe82* observations taken under non-photometric conditions, this kind of quality check is necessary to have a final stack of exceptional quality. Once the non-useful runs were rejected, we start the stacking process which is done in two steps. During the first step, we create shallow mosaics of equal size to the final mosaic from all the fields contained within a given run (or more in case we need to use several camera columns to cover the desired field-of-view). The mosaics are assembled from the sky-subtracted chips using SWARP (Bertin 2010b). Afterwards, we run SWARP over these shallow mosaics, applying a median stacking to all the available layers. It is important to note that the runs normally have slightly different offsets. Thanks to this, the scattered light from the telescope does not produce any pattern on the images either. Our final stacks do not show any residual sky-gradient or visible sky pattern. Due to the different number of layers used to compose the stacks, the mosaics have slightly different depths. Table 2 shows the number of layers used for the r'-band stacks (in brackets the number of g'-band layers, if that differs by more than 10%). For some of our galaxies, the u'-band and z'-band detector problems prevented us to create reliable mosaics. In these cases (NGC 1068, NGC 1087, UGC 02081, and UGC 02311 in the u'-band and NGC 1068 in the z'-band) we did not use the u'- and z'-band stacks for further analysis.

3.3. Photometric calibration

The photometric calibration of our deep mosaics is done by means of comparative photometry. The deep mosaics have an effective exposure time \sim equal to that of SDSS DR7. This makes it straightforward to compare number counts or surface brightness profiles to the DR7 calibrated data.

The SDSS DR7 photometric calibration is reliable at the level of $\sim 2\%$. We opted to follow the traditional recipe to determine the zeropoint of our stacks by using the *aa*, *kk*, and *airmass* (the photometric zeropoint, the extinction coefficient and the airmass coefficients). These

parameters are provided in the tsField table associated with the chip containing the target object. The surface brightness zeropoint can be given as $-2.5 \times (0.4 \times [aa + kk \times airmass] + 2.5 \times \log(t_{exp} \times pixelscale^2))$, where the pixelscale is $0.396''/\text{pixel}$ and the exposure time for each pixel equals to 53.907456 seconds.

We take the reliable part of the surface brightness profiles of our galaxies obtained from the DR7 imaging and match it to the corresponding part of the *Stripe82* surface brightness profiles. The mean difference is taken as a 'photometric' offset and applied onto the DR7 zeropoint: $ZP_{S82,x} = ZP_{DR7,x} + \Delta\mu_x$. Since the calibration is done in the same photometric filter system, no color term needs to be included.

3.4. Masking and Profile Extraction

We extract radial surface brightness profiles on masked mosaics in order to avoid contamination on our light profiles. We apply conservative masking onto sources which clearly do not belong to the galaxy, like foreground stars, background galaxies, etc. These sources are extracted by SExtractor from a master image composed of all 5 bands. This master image is a stack of the different filters scaled to the r-band flux. Sources are extracted in "cold mode", optimized for brighter objects. We use some SExtractor parameters such as the measured flux, elongation, and similar to determine the shape and size of these mask regions. Faint objects (fainter than ~ 20 mag) are not masked to statistically correct for the faint foreground stars unresolved from the galaxy image. In some cases, problematic sources, saturated stars, for instance, are masked manually. Since the masking is based on information coming from all 5 filters, we use the resulting mask as a mastermask, and it is applied to all filters.

In order to extract radial surface brightness profiles corresponding to the underlying outer disk, we need to get representative values of the ellipticity and position angle of this region. Taking a similar approach to SExtractor (Bertin & Arnouts 1996), we do this by computing the second-order moment of the light distribution of the galaxy using the DR7 r'-band image. The second-order moment is directly related to the position angle, the semi-major (A) and semi-minor (B) axis lengths. We fix this ellipticity and position angle for all elliptical apertures. In order to increase the signal-to-noise counteracting its natural decrement due to the lower surface brightness in the outer regime, we used a logarithmic radial sampling with steps of 0.03. In each aperture we estimate the galaxy flux by the $3\text{-}\sigma$ rejected mean of the pixel values of that aperture. This helps to minimize the effect of morphological features like a spiral arm crossing the aperture.

Our light profile, however, can still be contaminated by some residual sky background. This background is estimated by using equally spaced apertures. We obtain the number count profile of the galaxy up to very far distances, and we chose a large aperture where the profile becomes flat, beyond the identifiable profile of the galaxy. The $3\text{-}\sigma$ rejected mean of the fluxes inside this aperture gives a robust estimate of the residual sky background (for further information, see PT06, their Section 3.3). The error of the background determination is key to decide the surface brightness level down to which we trust our profiles. Following a conservative approach,

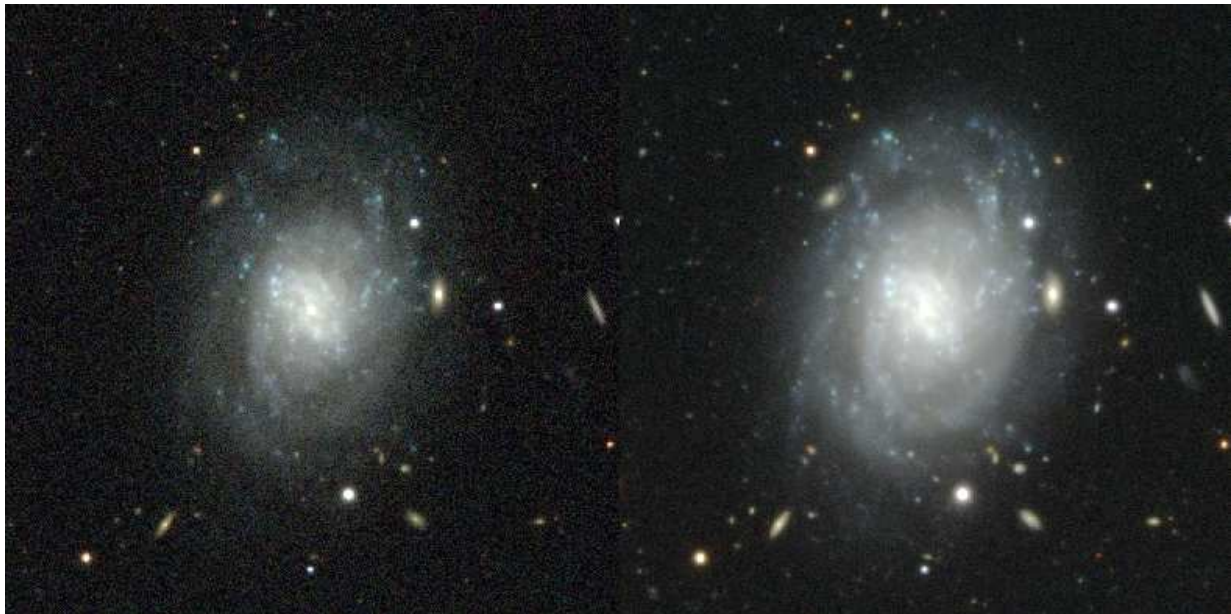


Figure 1. *Left:* RGB image of NGC 0941 created using the standard (single exposure) SDSS DR7 g' -, r' -, and i' -band imaging. *Right:* RGB image of NGC 0941 created using the g' -, r' -, and i' -band stacks of *Stripe82* exposures of NGC 0941. The *Stripe82* imaging is ~ 2 magnitudes deeper than the standard SDSS imaging, this effectively means that $S/N \sim 1$ on the SDSS DR7 imaging corresponds to features of a surface brightness equal to $25 \text{ mag arcsec}^{-2}$, however the same signal-to-noise on *Stripe82* imaging corresponds to $27 \text{ mag arcsec}^{-2}$.

this is placed where the profiles obtained by either over- or undersubtracting the sky measurement by $\pm\sigma$ start to deviate with more than 0.2 mag from the original profile. To see the limiting surface brightness of our profiles in the r' -band see Table 2.

3.5. Data quality

After stacking, *Stripe82* imaging is expected to be ~ 2 magnitudes deeper than the standard SDSS imaging. This amount of difference can be observed directly on the imaging: spiral galaxies show more outer structure, for instance, revealing outer disks extending farther out, meanwhile the inner morphology remains unchanged. As an example, see the DR7 and *Stripe82* RGB color composites of NGC 0941 on Figure 1.

A signal-to-noise ~ 1 per pixel on the DR7 imaging corresponds to features with a surface brightness of $\sim 25 \text{ mag arcsec}^{-2}$. However, by summing up thousands of pixels in the outer apertures of the surface brightness profiles, we can reach $S/N \sim 5$ at the level of $\sim 27 \text{ mag arcsec}^{-2}$. This is the S/N required to assure errors $\leq 0.2 \text{ mag}$. The same $S/N \sim 1$ per pixel on the *Stripe82* imaging can be associated with the surface brightness level of $\sim 27 \text{ mag arcsec}^{-2}$.

PT06 showed that with standard SDSS imaging it is possible to extract radial surface brightness profiles down to $\mu_{r'} \sim 27 \text{ mag arcsec}^{-2}$, hence we expect to be able to obtain reliable profiles down to $\mu_{r'} \sim 29 \text{ mag arcsec}^{-2}$. Table 2 shows that this depth is fairly stable for all our galaxies, however, in case of NGC 1068 or NGC 0941, due to a larger number of pixels falling in the outer apertures or smaller intrinsic noise thanks to better sky conditions, we were able to extract its profile down to $\mu_{r'} \sim 30 \text{ mag arcsec}^{-2}$.

These deep surface brightness profiles also prove the high quality of the regular SDSS imaging. We made a direct comparison between the r' -band profiles of NGC 0941 in Figure 2.

4. ANALYSIS

4.1. Surface brightness profiles

We obtained surface brightness profiles in all the five SDSS filters. These profiles are ~ 2 magnitudes deeper than regular SDSS profiles, giving way to explore the stellar populations of disks down to $\sim 0.5 M_{\odot} \text{ pc}^{-2}$. The deepest profiles, however, are obtained in the g' - and r' -filters, this is due to the better detector/filter response of these filters which results in smaller intrinsic noise. Due to this we explored in detail the r' -band surface brightness profiles and the $(g' - r')$ color. Our results can be found in the Galaxy Atlas for every galaxy separately (see Appendix A).

4.1.1. Classification

We used our deep r' -band surface brightness profiles to classify the surface brightness profiles of our galaxies. We followed the scheme presented in PT06 and Erwin et al. (2008). The surface brightness profiles of Type I galaxies are described by one single exponential, meanwhile Type II and Type III profiles both exhibit a well defined feature called the break. After an exponential decline, Type II profiles are followed by a downbending-, Type III profiles with an upbending-exponential after this inflection point. There exist several sub-classes of Type II profiles, related to the possible origin of the break. We distinguish the so called *Outer Lindblad Resonance* breaks (Type II-ORL), for these galaxies the break in the surface brightness profile lies close to the resonance zone caused by the bar, at ~ 2 times the bar radius. In case the break cannot be associated with such a well-defined phenomena, it is classified as *Classical Truncation* (Type II-CT). We show the results of our classification in Table 4.

4.1.2. Excess of light at $\mu_{r'} \sim 28 \text{ mag arcsec}^{-2}$

The surface brightness profiles of our seven galaxies can be fitted into the aforementioned basic scheme. However,

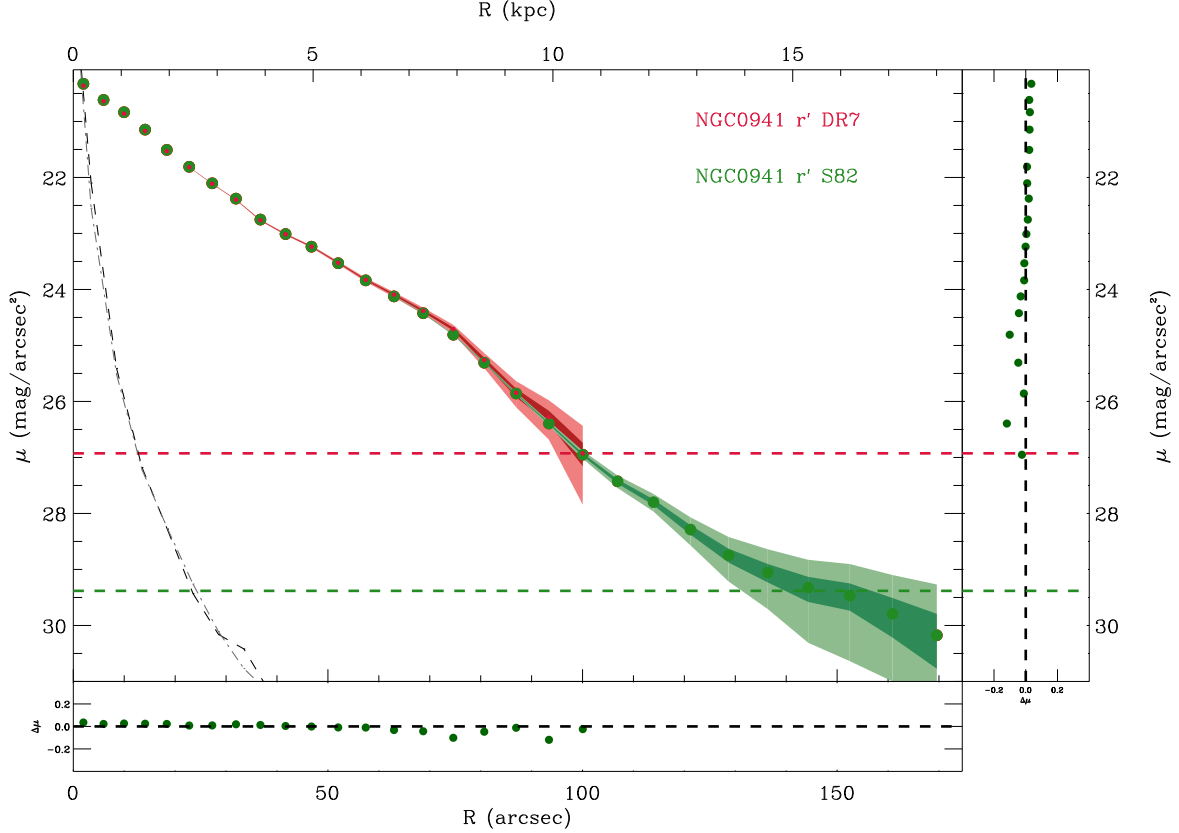


Figure 2. Comparison of the surface brightness profiles of NGC 0941 obtained from standard SDSS DR7 imaging and *Stripe82* stacks. In red we plot the surface brightness profile obtained from the standard SDSS imaging, the *Stripe82* profile is overplotted in green. The shaded regions indicate the 1 and 3 σ under- and over-subtracted profiles in both cases. The surface brightness limits of our profiles are placed where the 1 σ under- and over-subtracted profiles start to deviate by more than 0.2 magnitude from the original profile. The DR7 limiting surface brightness (26.9 mag arcsec $^{-2}$) is indicated by the red dashed line, the *Stripe82* limiting surface brightness (29.4 mag arcsec $^{-2}$) is indicated by the green dashed line. On the joint panels we plotted the deviation of the DR7 profiles from the *Stripe82* profile against the surface brightness and radius, this deviation is well below 0.2 magnitudes. This is a further proof of the reliability of the standard SDSS imaging. *Stripe82* PSF: we also draw the PSF profiles of the g'- and r'-band imaging scaled to the r'-band central flux of NGC 0941. We observed no anomalous color gradient of the PSF.

we note that most of our galaxies exhibit some extra light above the outer disk expectations starting at ~ 28 mag arcsec $^{-2}$. This extra light follows a flattened profile that we think is not associated with any morphological feature belonging to the outer disk. In fact, in this paper, we work under the hypothesis that this extra light is diffuse light from the stellar halo. This extra light appears and shows the same structure in the other deep SDSS bands (g' and i'), as well.

To further check our hypothesis, we investigated the origin of these features. First, we had to be sure that no artifact due to observational errors could possibly affect the quality of our profiles. There are several known problems related to integrated photometry like flat-fielding, skysubtraction, contribution by saturated stars or extended PSFs which could cause artificial excess (or defect) on our light profiles.

Flatfielding— SDSS imaging due to their drift-scan technique used during the observations show no evidence of flatfielding issues.

Skysubtraction— On our surface brightness profiles we already took into account the possible effect of an error in the estimation of the background. We drew shaded

regions corresponding to the 1 σ and 3 σ under- and over-subtracted profiles (see Appendix A). The turnup point of the stellar halo feature (typically at $\mu_{r'} \sim 28$ mag arcsec $^{-2}$) is at a surface brightness level $\geq 15\sigma$ above the sky level. The fact that we also see the same behavior for all the galaxies and in different bands, reinforces the idea that this is a real feature.

Saturated stars— There is only one galaxy, NGC7716, where there is significant contribution from a saturated star that makes the interpretation of our surface brightness profile harder. This, however, could be minimized by extensive masking over the galaxy disk itself. We assessed the size of the region affected by scattered light by obtaining a pseudo surface brightness profile of this saturated star. We used similar approach to check the effect of saturated stars in case of other galaxies.

Scattered light from the bulge— Given the depth of our images, we might expect the effect of the PSF on the bulge (the sharpest feature) of our galaxies to have a significant contribution at low surface brightness levels in form of an extended wing. This could cause the bulge light to scatter far enough to affect the surface brightness

profiles in the outer regions. To check the shape of the PSF at low surface brightness levels, we need to model accurately the PSF of the stacks. We used again PSFex to create the models of the PSF of our stacks. These PSF models are usually ~ 12 magnitude deep and might extend over ≤ 50 pixels. By scaling these PSF models to the central surface brightness of the galaxy (see Figure 2), we have seen that the extension and depth of the PSFs is negligible and could not affect the outer disk profiles. (We also considered the possibility of the bulge emerging above the disk, as a cause to observe the upturns on these profiles. Some arguments have been made in recent years that Type III profiles, that exhibit an excess of light over the disk in the outer regions, can be associated with the bulge emerging above the disk. The features we observe on the surface brightness profiles are a bit akin to Type III behavior, although in late-type spirals it would be somewhat unexpected to find bulges reaching ~ 10 kpc or farther out.)

After checking the above issues, we are confident that the excess of light observed at $\mu_{r'} \sim 28$ mag arcsec $^{-2}$ is real. We compared the surface brightness levels of our galaxies to several nearby galaxies like Andromeda (M31), M33, M81, or NGC2403. These galaxies are known to have well studied faint structures which were identified by several independent groups using 'resolved star' technique (e.g. Ferguson et al. 2002, 2007; Ibata et al. 2007; McConnachie et al. 2009; Barker et al. 2009, 2012). The base of our comparison is that our galaxies have quite similar stellar masses. Courteau et al. (2011) showed that the regime of stellar halos actually starts at the level of $\mu_I \sim 27$ mag arcsec $^{-2}$ (using the color predictions³ of Vazdekis et al. 2010 for old and metal-poor stellar populations, this magnitude translates into $\mu_{r'} \sim 27.5$ mag arcsec $^{-2}$) corroborating our assumption of observing the signs of stellar halos on our profiles.

4.1.3. Deriving disk and stellar halo parameters

In addition to the classification of the surface brightness profiles, we carried out a detailed structural analysis on the observed r' -band profile. To derive reliable parameters of the disk and stellar halo, a Bulge/Disk/Stellar Halo decomposition was done by simultaneously fitting each component. With this we also avoid overestimating the light contribution of the different components, especially that of the stellar halo to the total galaxy light. We fitted a composite model built up from functions corresponding to the known or assumed shapes of the different morphological components observed on the profile. It has been known for some time that disks are well fitted with exponential profiles (Patterson 1940; Freeman 1970). However, the majority of disks does not follow a single exponential profile, but rather exhibits light deficiency or in some cases excess in the outer disks (van der Kruit 1979; Erwin et al. 2005, 2008, PT06) after a well identifiable point of the profile, which is often called the *break radius*. Due to these reasons, we modeled the disk by a double-exponential to take into account the existence of these breaks:

$$I(R) = I_{0,1}e^{R/h_1}\Theta(R_{br}) + I_{0,2}e^{R/h_2}(1 - \Theta(R_{br})). \quad (1)$$

³ See also on <http://miles.iac.es>

The central intensity of the inner and outer disks are $I_{0,1}$ and $I_{0,2}$, and $\Theta(R_{br})$ is the step function:

$$\Theta(R_{br}) = \begin{cases} 1 & \text{if } R \leq R_{br} \\ 0 & \text{if } R > R_{br}. \end{cases} \quad (2)$$

The step function assures the double-exponential profile with h_1 and h_2 scalelengths before and after R_{br} break radius.

The bulges of spiral disks are modeled with an $r^{1/n}$ profile (Andredakis, Peletier, & Balcells 1995). The 1D Sérsic $r^{1/n}$ -profiles (Sérsic 1968) can be written as follows:

$$I(R) = I_e \exp \left\{ -b_n \left[\left(\frac{R}{R_e} \right)^{1/n} - 1 \right] \right\}, \quad (3)$$

where R_e is the effective radius, and $I_e = I(R_e)$. The quantity b_n is a function of the shape parameter n , and is chosen so that the effective radius encloses half of the total luminosity, a good approximation can be given as $b_n \sim 2n - 0.324$ (e.g. Graham 2001).

Stellar halo profiles obtained by star-counts method are often fitted by Sérsic-profiles, as well, (see e.g. Courteau et al. 2011).

Altogether, the composite profile has 10 free parameters that needs to be fitted. In addition to this, in the flat, outer region where the stellar halo dominates the profiles, the observational errors are playing a significant role. Due to this, and after visual inspection, we decided to minimize the uncertainty in determining the properties of the stellar halo by fixing its shape with a Sérsic index $n = 0.5$, that is a Gaussian profile. Trujillo et al. (2002) showed that the mass density profile of the $r^{1/n}$ family can be extremely well approximated by an analytical expression (see their Eq. 7), which yields an exact case for $n = 0.5$. By choosing this constraint therefore we ensure a moderately declining mass distribution, on the other hand allowing a higher value for the Sérsic-index would mean that the stellar halo has a prominent "over the disk component" in the inner parts of the galaxy (see their Fig. 2).

The profile fitting is performed with the *MPFIT* routine in the Interactive Data language (IDL), this routine is based on the Levenberg-Marquardt algorithm (Markwardt 2009) to carry out non-linear least-squares minimization. Although this fitting method is extremely sensitive to initial conditions, with a proper set of input parameters the algorithm gives excellent results.

The decomposition of the light profile yields robust estimation of the scales of different galaxy component, like disk scalelengths and halo effective radius, that can be directly compared to theoretical expectations, and it also becomes possible to compare these halos to that of the Milky Way or M31. In case of the Local Group galaxies it becomes possible to integrate the observed *starcoun*t profile out to large radii, obtaining a robust and model-free estimation on the contribution of the halo light to total galaxy light. In our case, we only trace the inner part of the stellar halo, hence we cannot estimate the halo contribution by simple integration. However, one advantage of using Sérsic models (as it is shown e.g. in Trujillo, Graham, & Caon 2001) is that the global prop-

erties, such as the total light (L_T) and the mean effective surface brightness ($\langle\mu\rangle_e$), can be given in the form of exact analytical formula based on the aforementioned three observables (n , R_e , and I_e):

$$L_T = k_L I_e R_e^2, \quad (4)$$

where k_L is the “structural parameter” that depends on the Sérsic index:

$$k_L = e^{b_n} \frac{2\pi n}{b_n^{2n}} \Gamma(2n), \quad (5)$$

and

$$\langle\mu\rangle_e \equiv -2.5 \log \frac{L_T}{2\pi R_e^2}. \quad (6)$$

The evaluation of the total galaxy light is as follows: we integrate the observed profile until the last measured point. Outside this region (to take into account the stellar halo contribution) we extrapolate the behavior of the fit of stellar halo to infinity. The stellar halo light fractions of the 7 galaxies compared to the host galaxy luminosity are shown in Figure 3.

4.2. Stellar Population Analysis

4.2.1. Color Profiles

In addition to the light distribution of these late-type spirals we obtained color profiles to explore the radial distribution of stellar populations in our galaxies. Normally, color profiles cannot be studied down to the same surface brightness level as the surface brightness profiles, due to the fact that errors propagate quadratically and the uncertainty of the color is necessarily attributed to the uncertainty of the sky estimation in both filters. The errors coming from the sky estimation, however, can be alleviated by using large bins. We find that the most convenient strategy is to place the color bins around the well identified morphological features such as the bulge, disk etc. Nevertheless, it is important to avoid using a single bin to describe regions where the color gradient is steep, and it would mean mixing very different stellar populations. The bins we applied for the g'-r' color profiles (see Appendix A) are a compromise between the increase of signal-to-noise and underlying color gradient.

In the regime of the stellar halo we observe no significant color gradient, therefore to give a robust result, we obtained a single (g'-r') color for our stellar halos using one large bin. To derive these colors for all stellar halos in a consistent way, we placed the inner boundary of the color bin at the radius ($R_{>50}$) where the stellar halo light starts to dominate the total light, and the outer boundary at the radius where the surface brightness profile reaches the 3σ skynoise. This way the binsize depends on the stellar halo properties and intrinsic noise properties of the image.

We also obtained color profiles for other adjacent filters (u'-g', r'-i', i'-z'), in total providing 4 color profiles that can be studied in detail.

The Galactic extinction has been taken into using the Schlegel et al. (1998) values. We used the IDL code provided by Schlegel et al.⁴ to get the values corresponding

to the different galactic positions of our sample.

4.2.2. Color errors

Deriving colors for the faint stellar halo calls for a lot of care. At very faint surface brightness levels, the colors are affected by the shape of the PSF of the different bands. Anomalous PSF scattering can cause excess of light in one band, hence causing an artificial color. This effect was presented e.g. by de Jong (2008) who accurately proved that (1) PSF tails on stacked SDSS imaging can extend as far as ~ 100 pixels reaching ~ 14 magnitudes below the central surface brightness, (2) color gradients and reddening could be artificially caused by the extended scattering especially in the SDSS i'-band.

Particularly, in the case of edge-on galaxies (Zibetti et al. 2004; Zibetti & Ferguson 2004), according to the de Jong (2008) results, the scattered light from the central disk contaminates the light of the stellar halo. In face-on projections, however, the artificial color gradient induced by the different wing extensions of the PSF plays a less relevant role. This is for two reasons: (1) the slope of the surface brightness profiles in face-on projections are much moderate than in the edge-on case being less affected by the PSF; (2) whereas the stellar halos are found after the disk immediately in edge-on projections, in face-on projections the transitions are much moderate and the PSF size is not large enough to affect the stellar halo in their outer regions.

Colors could also be affected by an inaccurate sky subtraction. To account for the propagation of the uncertainty of the sky estimation into the color, we over- and undersubtracted the galaxy images with 1σ uncertainty, and obtained total intensity, hence magnitudes in the different bins from those images. The mean magnitude difference $\langle\delta\rangle = |m_{+\sigma} - m_{-\sigma}|/2$ was propagated quadratically:

$$\Delta = \sqrt{\langle\delta\rangle_g^2 + \langle\delta\rangle_r^2}$$

and used as error on the color.

4.2.3. Stellar surface mass density profiles

To study the stellar mass distribution of our spirals, we computed the stellar mass density (Σ_*) profiles using the Bell et al. (2003) prescriptions for the mass-to-light (M/L) ratio.

In this work we assume a Kroupa IMF (Kroupa 2001), which according to Bell et al. (2003) implies a deduction of 0.15 dex from the mass-to-light ratio using the following expression:

$$\log_{10}(M/L)_\lambda = (a_\lambda + b_\lambda \times color) - 0.15, \quad (7)$$

where for the SDSS (g'-r') color $a_\lambda = -0.306$ and $b_\lambda = 1.097$ is applied to determine the r' band M/L .

Once we know the (M/L) ratio, using the expression below it is straightforward to link the stellar mass density (Σ_*) profile with the surface brightness profile at a given wavelength (μ_λ).

$$\log_{10}\Sigma_* = \log_{10}(M/L)_\lambda - 0.4(\mu_\lambda - m_{abs,\odot,\lambda}) + 8.629, \quad (8)$$

where $m_{abs,\odot,\lambda}$ is the absolute magnitude of the Sun at wavelength λ , and Σ_* is measured in $M_\odot \text{pc}^{-2}$.

⁴ <http://astro.berkeley.edu/~marc/dust/index.html>

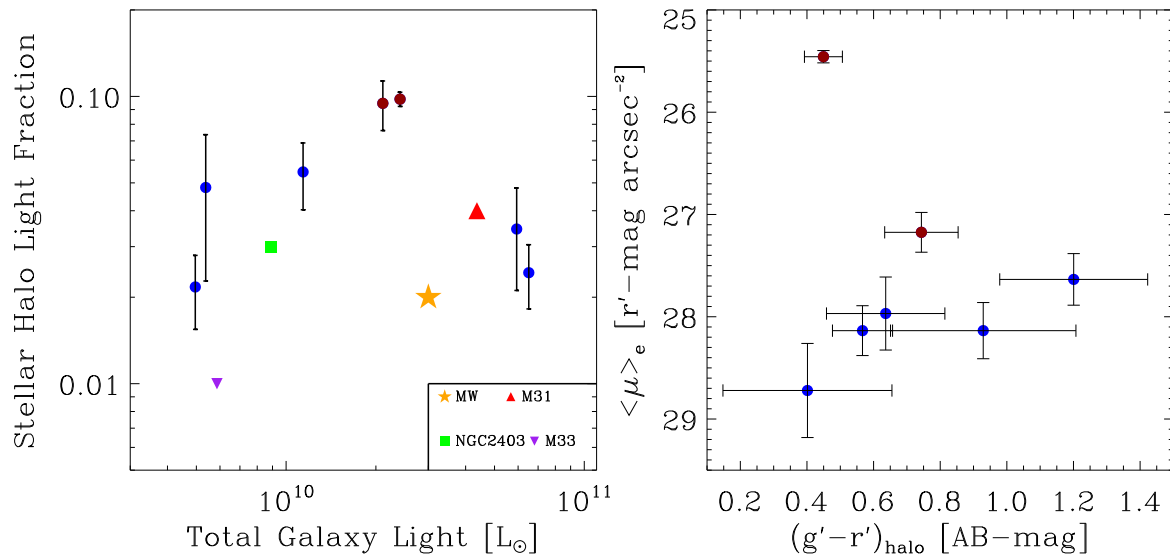


Figure 3. *Left panel:* Fraction of the stellar halo light vs. the total galaxy light. The stellar halo light is estimated by fitting with a $n=0.5$ Sérsic-mode the region of the stellar halo of the galaxies, meanwhile to obtain the total galaxy light we integrated the observed profile. The dark red points coincide with the galaxies where we identify the presence of tidal features (*NGC7716*) or minor mergers (*NGC1087*). The stellar halo light fraction observed in the Milky Way (Carollo et al. 2010), M31 (Courteau et al. 2011), M33 (McConnachie et al. 2010) and NGC2403 (Barker et al. 2012) are also overplotted. The light contribution of the stellar halo to the total galaxy light varies from $\sim 1\%$ to $\sim 5\%$, but in case of ongoing mergers the stellar halo light fraction can be as high as $\sim 10\%$. *Right panel:* Effective surface brightness of the stellar halo vs. the integrated $(g'-r')$ color of the stellar halo. When computing the stellar halo color, the halo region is taken outside the radius where the halo light start to contribute with $\geq 50\%$. We find colors ranging $(g' - r') \sim 0.4 - 1.2$. The extremely red halo colors ($g' - r' > 0.8$) are found in galaxies with no evident interaction.

4.3. Stellar population models

Comparing the observed stellar halo color to the predictions of single stellar population (SSP) models we expect to get a crude hint on the stellar population that might build up the observed stellar halos. Since we lack a wide multiwavelength data, we opted for constraining the observed $(g'-r')$ colors. We used the latest MILES SSP models. These empirical models are based on real stellar spectra and give excellent coverage both for metallicity and ages (Vazdekis et al. 2010). Another important aspect of using these models is that they provide predictions for different IMFs.

We have decided to constrain the stellar populations of the stellar halos in a novel way. This was necessary since the age-metallicity degeneracy prevents us to gain a deeper understanding of these stellar populations, moreover we would like to see how the observational errors affect the measurements of age and metallicity. To this end we created synthetic color maps based on the Vazdekis models.

As a first step, we took all SSP model spectra and convolved them with the SDSS g' and r' filters in order to compute model colors for each age and metallicity. Then we composed a two-dimensional map of the model colors and placed our measurements over the age-metallicity grid. To visualize how the age-metallicity degeneracy appears in the colors of the stellar population, we assigned the colors of the rainbow table in IDL to the values computed from the models. The rainbow colors change smoothly from violet(black) to red. Instead of computing χ^2 values from the observed colors, we decided to use the observed colors and its errors, directly on these maps. The range of colors within the observed color and

its error bar can be associated with a range of ages and metallicities, creating by default a two-dimensional problem. This is shown in Figure 4.

We have found that some of our observed stellar halo colors are so red, that they lay outside the grid of models based on the conventional Kroupa IMF with slope $\alpha = 1.3$. The observed halo colors are redder than the reddest colors of those models. Redder model colors can be expected of models based on bottom-heavy IMFs (Vazdekis et al. 2010). Although, there is a wide range of IMF slopes between $\alpha = [0.3, 3.3]$ available, here, we simply took the model that provided us with the reddest colors, therefore we used models with Unimodal IMF with a slope of $\alpha = 3.3$. To comprehend how the IMF affects the intrinsic color distribution, see Figure 4.

5. RESULTS

5.1. Surface brightness profiles

The surface brightness profiles of our 7 galaxies have been classified accordingly to the scheme explained in Section 4.1.1.

Our sample contains one Type I disk NGC 1068(=M77). In this work, NGC 1068 has been classified as Type I (in PT06 it was classified as Type II-ORL). We considered here that rather than having a break associated with the Outer Lindblad Resonance cited by PT06, the extended oval distortion in the disk accounts for the extra light over the disk observed on the surface brightness profile (see Figure 10). NGC 0450, NGC 0941, and UGC 02081 exhibit Type II classical truncations, the break of UGC 02311 lies by the resonance zone caused by a bar, hence it is classified as Type II-ORL. When classifying NGC 1087 and NGC 7716, we had to be a bit cautious. These

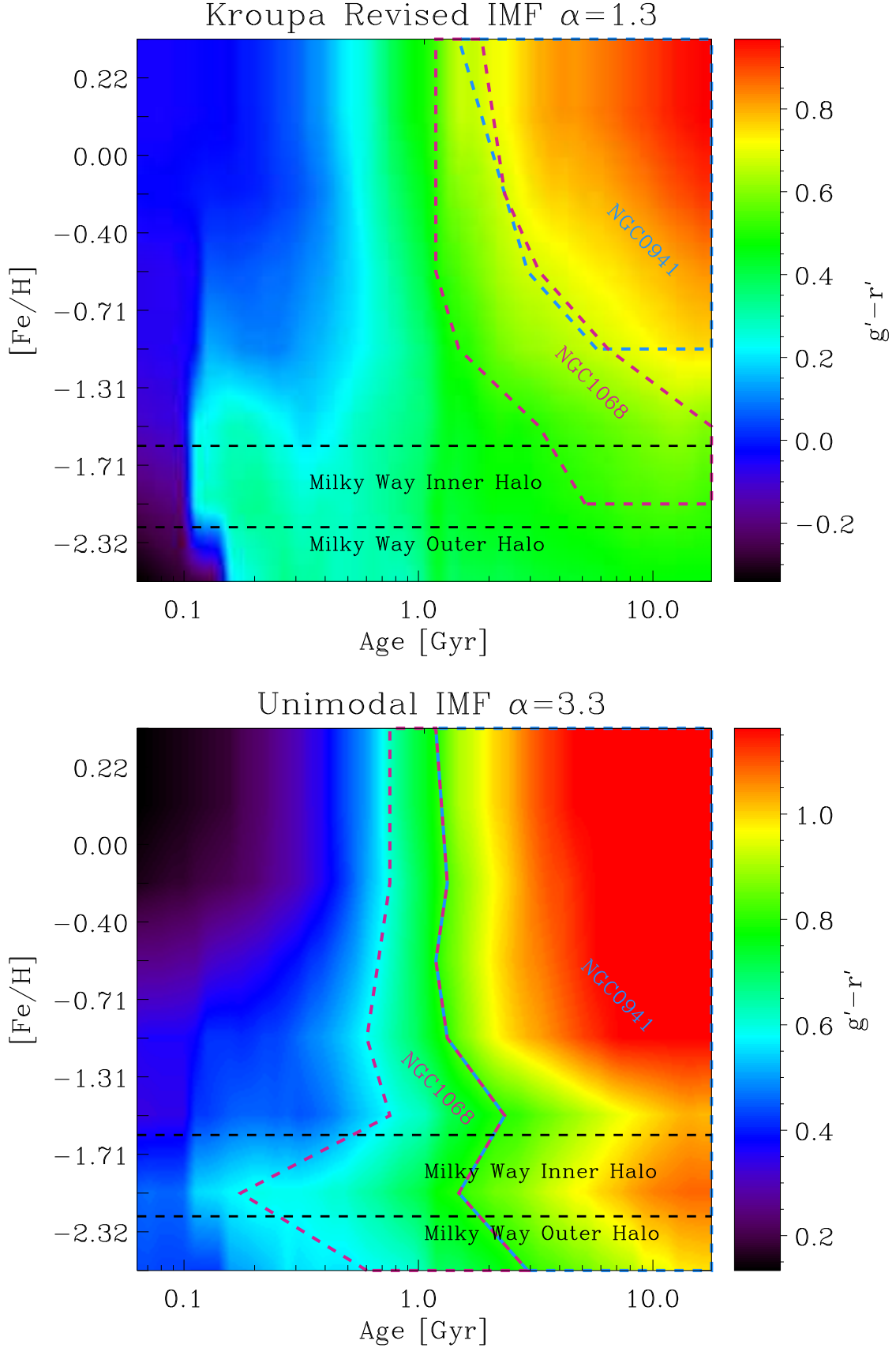


Figure 4. Metallicity-Age maps: Using the MILES SSP models (Vazdekis et al. 2010) to get a hint on what stellar populations might build up the stellar halos. We illustrate the expected age and metallicity for two different galaxies. In case of NGC 0941 the stellar halo is extremely red and models produced by regular Kroupa IMF are unable to reproduce this color. The blue (NGC 0941) and magenta (NGC 1068) dashed lines show the age and metallicity solutions that are compatible with the observed colors within their error bars. The upper panel displays the model colors for Kroupa IMF and the bottom panel with a bottom-heavy IMF.

Table 3
Bulge Properties

Galaxy	n	$R_{e,b}$ [kpc]	$\mu_{e,b}$ [mag arcsec $^{-2}$]
NGC0450	0.95	0.94	20.77
NGC0941	0.64	1.34	21.73
NGC1068	0.92	0.54	16.54
NGC1087	0.73	0.24	17.81
NGC7716	1.50	0.60	18.18
UGC02081	0.50	0.45	20.49
UGC02311	1.33	4.18	20.21

galaxies seem to have a break feature in the inner disk that can be associated with a centrally more concentrated star forming region. This however is not the kind of phenomena we designate as Type II, hence these galaxies are classified as Type II*. In their outer disk both galaxies exhibit Type III up-bending. In NGC 7716 this extended Type III feature has a disk origin starting at about 80 arcseconds at a level of 25 mag arcsec $^{-2}$, meanwhile in NGC 1087 the up-bending shows a spheroidal origin. To be consistent with previous classification scheme, these 2 galaxies have been classified as Type II+III.

Interesting to note that the high contribution of the stellar halo light in case of NGC 1087 explains why this galaxy in PT06 was classified as Type III. However, in this sample, we find that the presence of the stellar halo causes a “Type III like” feature on all profiles.

Beyond the classification, we derived several properties related to the radial light distribution of these galaxies. Applying the decomposition explained in Section 4.1.3, we inferred several structural properties for the bulge, disk, break, and stellar halo.

5.1.1. Bulge properties

This paper was not aimed to discuss bulges in detail, however, it is interesting to note that the bulges of our galaxies are well fitted with low Sérsic-index(n) values $n \lesssim 1.5$ (see Table 3). Kormendy & Kennicutt (2004) discussed that small n values are signatures of pseudo-bulges. There is also a general trend noted by Andredakis, Peletier, & Balcells (1995) that in late-type (Sc and later) galaxies the bulge profiles are very close to being pure exponentials. We observe the same trend for our objects, and that indeed in some cases, like NGC 0941, we have alternatively confirmed the presence of a pseudo-bulge (Kormendy, private communication).

5.1.2. Disk and Break properties

Our model fitting provides robust estimations of disk properties, such as inner, and outer scale-lengths, break radius, inner and outer disk central surface brightness, and the break surface brightness. The results of the fitting can be found in Table 4. A detailed statistical analysis of these parameters is beyond the scope of this paper, due to the low number of observed galaxies in our sample. However, on a one-by-one basis it is interesting to compare their properties to previous studies of late-type disks, and later on, to put this in context with the observed stellar halo properties.

PT06 studied ~ 90 galaxies where they have found that $\sim 60\%$ of late-type disks contain Type II breaks.

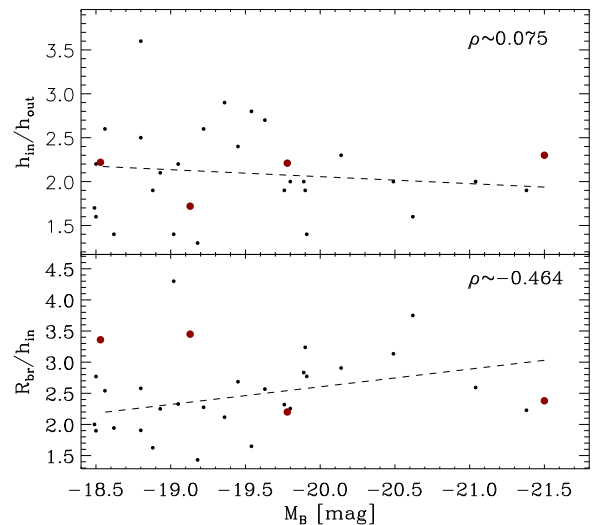


Figure 5. Disk property correlations with absolute magnitude for the PT06 Classical Truncation sample. The red dots are the properties obtained for the Type II galaxies of the current sample. Overplotted in both panel are robust linear fits to guide the eye and in the upper right corner the Spearman rank correlation coefficient. *Upper panel:* The inner and outer disk scale-length ratio for the PT06 sample of Type II-CT galaxies. *Bottom panel:* The break radius in inner scale-length units.

Based upon this result it is not surprising that four of our seven galaxies ($\sim 60\%$) exhibit Type II behavior. PT06 also studied the typical radius where surface brightness breaks usually occur, taking into account that the morphologically distinct sub-classes might have very different origins. Five of our galaxies (NGC 0450, NGC 0941, NGC 1068, NGC 1087 and UGC 02081) were part of the PT06 sample, as well. Besides of the re-classification of NGC 1068 and NGC 1087, the break radii we measured for NGC 0941 ($R_{br} \sim 72''$) and UGC 02081 ($R_{br} \sim 67''$) are different from the PT06 values ($R_{br} = 82''$ and $53''$, respectively). Part of these differences are due to the different ellipticities we applied when obtaining the surface brightness profiles. Different ellipticity means different scale-length properties, as well. However, differences in the measurement of the scale-length might also arise due to a more accurate Bulge/Disk decomposition method we used to infer disk properties. We nevertheless are in position to say that statistically the obtained break properties are within the PT06 expected ranges. In light of both results, we conclude that the method applied in PT06 was sufficient to give constraints on the disk structure on a statistically significant level, and that the use of shallow DR7 data does not compromise disk measurements.

Similarly to PT06, we characterized the strength of the break by the ratio of the inner and outer scale-lengths. The mean ratio of the inner and outer scale-length on the PT06 sample was 2.5 ± 0.5 . They also reported a lower range of values that could be as low as 1.1 (case of NGC7716). To compare how our measurements fit into the PT06 relations, we overplotted the $\frac{h_{in}}{h_{out}}$ of this paper with the PT06 values (see the upper panel of Figure 5).

PT06 showed that Type II Classical Truncations

Table 4
Disk and Break Properties

Galaxy	SB-Type	R_{break}			h_{in}		h_{in}	$\mu_{0,in}$	$\mu_{0,out}$	μ_{br}	$(g' - r')_{br}$	Σ_{br}
		[$''$]	[kpc]	[h_{in}]	[$''$]	[kpc]	[h_{out}]	[mag arcsec $^{-2}$]				[$M_{\odot} pc^{-2}$]
NGC0450	Type II-CT	82.3	9.7	2.20	37.4	4.4	2.21	21.19	18.29	23.53	0.26	8.2
NGC0941	Type II-CT	71.5	7.6	3.45	20.7	2.2	1.72	20.82	18.13	24.50	0.35	4.2
NGC1068	Type I	71.5	5.3	...	20.91
NGC1087	Type II*+III	51.4	5.2	1.37	37.4	3.8	1.65	19.77	18.81	21.17	0.39	98.8
NGC7716	Type II*+III	39.2	6.9	2.53	15.5	2.7	1.10	19.85	19.59	22.47	0.40	30.8
UGC02081	Type II-CT	66.5	11.8	3.36	19.8	3.5	2.22	21.60	17.16	25.32	0.28	1.7
UGC02311	Type II-ORL	42.1	21.0	2.38	17.7	8.8	2.30	21.47	18.11	23.92	0.43	8.8

(NGC 0450, NGC 0941 and UGC 02081) are expected to occur at $\sim 9 \pm 2.4$ kpc, meanwhile breaks related to resonances (UGC 02311), show a wider span of galactocentric distances with the same mean distance (~ 9 kpc). Both distributions showed the tendency of larger break radius occurring in higher luminosity galaxies (see their Figure 7). Taking into account their results, it is not surprising to measure such a large break radius in UGC 02311, since this galaxy is ~ 2 -3 magnitudes brighter than the other galaxies with Type II-CT breaks (see Table 1). The break radius measured in relation to the scale-lengths, however, does not reveal such differences between the two Type II sub-types, its typical value being 2 -3 h_{in} , this matches well with the mean parameter value of 2.5 ± 0.6 found in PT06 (see lower panel of Figure 5). The inner scale-lengths of these galaxies correspond to the typical values measured in local galaxies (de Jong 1996; MacArthur et al. 2003), although UGC 02311 has a scale-length larger than usual (~ 9 kpc).

The inner disk central surface brightnesses are ~ 0.5 magnitude fainter compared to the PT06 values. This difference could be attributed to the better treatment of the light contribution from the bulge done in this paper. The wider spread deviations in the outer disk central surface brightnesses compared to the PT06 values are more difficult to explain. The proper fitting of the stellar halo should in any case cause the outer disk scale-length to shorten and its central surface brightness to brighten, resulting in a sharper break. However, PT06 breaks appear to be sharper (having brighter central surface brightnesses, and larger h_{in}/h_{out}), probably the effect of the ellipticity, that we intend to investigate in our upcoming paper (BT2012, in prep.).

In order to investigate how Type II break properties (namely the inner and outer scale-length ratio) depend on the observing wavelength, we carried out a Bulge/Disk decomposition on the profiles in all 5 filters (if available) by applying the bulge and disk part of the fitting routine explained in Section 4.1.3. To be fully consistent, we fitted the same disk region for all filters for our galaxies. We have cut the profiles taking care of not mixing the regions where the stellar halo light would have a significant contribution. During the fit we fixed the break radius.

We find that the h_{in}/h_{out} decreases smoothly from u'- to z'-bands in our Type II galaxies (see Figure 6).

5.1.3. Stellar Halos

Using SDSS *Stripe82* data gives us the opportunity to study the stellar content of disk galaxies down to a very deep level ~ 30 mag arcsec $^{-2}$ in the r'-band. This depth enables us to get a glimpse of the stellar halo on the surface brightness profiles: the light contribution from the stellar halo leaves a well identifiable upturn on the r'-band profiles, and when the stellar halo starts to dominate the light the profile becomes flatter. We observe this flattening on the profiles of all 7 galaxies that helped us to establish that the typical surface brightness level at which stellar halos start to affect the shape of the surface brightness profiles is ~ 27 mag arcsec $^{-2}$.

Although, this is a purely observational concept, it is interesting to discuss the radius where the light profile of the (outer) disk of the galaxy *first* starts to deviate from the exponential decline. We refer to this radius as the turn-off radius ($R_{turnoff}$) in Table 5. The estimation of this radius (and surface brightness) is model-dependent. Based on the assumption that the disk continues exponentially without having an actual edge, a 0.5 magnitude change (larger than the error bars of our measurements at these levels) could be expected if the halo light contribution reaches $\sim 25\%$ that of the disk. This 0.5 mag

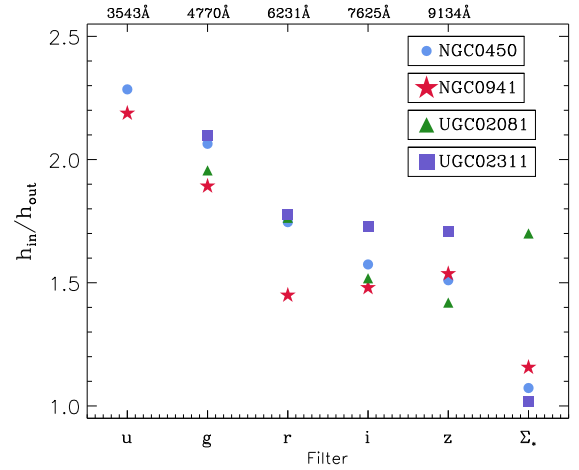


Figure 6. The strength of the break (indicated with the inner-outer disk scale-length ratio) obtained from the surface brightness profiles observed in the 5 SDSS bands and from the stellar surface mass density profile (See 4.2.3). The inner-outer scale-length ratio decreases rapidly towards the redder filters, moreover on the stellar surface mass density profile the break disappears ($h_{in}/h_{out} \sim 1$). However, in case of UGC02081 the break remains prominent on the stellar surface mass density profile, implying that the break in this galaxy is entirely different phenomena and resembles more of the cut-offs found by van der Kruit (1979).

Table 5
Properties of stellar halos

Galaxy	R_e	$\langle\mu\rangle_e$	$R_{turnoff}$			$R_{>50}$	
	[kpc]	[mag arcsec $^{-2}$]	[$''$]	[kpc]	[h_{in}]	[$''$]	[kpc]
NGC0450	18.90	27.64	128.68	15.22	3.44	152.48	18.04
NGC0941	9.90	28.14	100.05	10.62	4.83	121.20	12.87
NGC1068	38.00	28.14	393.82	29.21	5.51	513.78	38.11
NGC1087	13.50	25.46	111.46	11.19	2.98	159.11	15.97
NGC7716	35.00	27.74	86.96	15.39	5.61	106.89	18.91
UGC02081	20.11	28.72	84.08	14.88	4.25	97.36	17.23
UGC02311	40.00	27.97	62.98	31.39	3.56	74.62	37.19

deviation from the expected exponential shape of the surface brightness profile is well observable. The measured values of $R_{turnoff}$ fall at 10 to 30 kpc from the center of the galaxy, in terms of the inner scale-length between 3 and $5.5 h_{in}$.

These upturns should not be confused with the outer regions where the stellar halo clearly dominates the light of the galaxy (since around the upturn the disk is still the major contributor of the galaxy light). The radius where more than 50% of the galaxy light comes from the stellar halo is referred as $R_{>50}$. At this radius the stellar halo contribution clearly overcomes that of the disk and dominates the flat appearance of the surface brightness profile. As it is seen in Table 5, there are, on average, 2-3 kpc differences between $R_{turnoff}$ and $R_{>50}$.

In all these aspects, NGC 1087 is a special case. In this galaxy the stellar halo starts to affect the shape of the surface brightness profile at higher surface brightness levels. Our results imply that NGC 1087 has an unusually bright stellar halo with $\langle\mu\rangle_e \sim 25.5$ mag arcsec $^{-2}$. Probably this is the reason why this galaxy, based on shallow surface brightness profiles (see PT06), was classified as Type III. This altogether raises an important question: just how many (late-type) galaxies classified as Type III are in reality Type I galaxies with a bright stellar halo?

The mean effective surface brightness ($\langle\mu\rangle_e$) of our stellar halos have a typical value of ~ 28 mag arcsec $^{-2}$ (see Table 5). NGC 1087 and NGC 7716, the two interacting galaxies have brighter $\langle\mu\rangle_e$ (see Table 5).

An important aspect of our study is the light fraction contained within the stellar halo compared to the total stellar light of the galaxy. We find fractions in the range of 1–5%. These are typical values observed in nearby galaxies, as well. In two galaxies (NGC 1087 and NGC 7716), though, the light fraction of the stellar halo reaches nearly $\sim 10\%$. It is interesting to note that in both galaxies we note signs of ongoing interaction or merging. NGC 7716 is a clear-cut example of tidal streams surrounding a galaxy (see Figure 7), that appears as a sharp feature on the surface brightness profile, and has a surface brightness of ~ 26.5 mag arcsec $^{-2}$.

There could be several candidates as progenitors for this tidal stream(s), but due to lack of spectroscopic data we cannot decide whether the objects along the stream do indeed belong to the system or are only background objects. There is only one known satellite of this galaxy reported (Zaritsky et al. 1993), but that is found too far (at a projected distance of ~ 130 kpc) to be connected to the streams. NGC 1087 is not such an obvious case of interaction, but a misaligned outer disk might indi-

cate that the equilibrium of the disk has been disturbed recently by an external source.

5.2. Color profiles

The u', g', r', i', and z' filters of SDSS give a full coverage of the Spectral Energy Distribution (SED) in the optical regime. In principle, using all the five filters gives us the opportunity to learn whether the surface brightness distribution and color gradients exhibit any kind of dependence on the observing wavelength allowing us to constrain the stellar populations responsible for the energy output in the different galactic components. Unfortunately, not all bands behave as well as g' and r'. Stacking u', i', and z'-band data did not result in such exceptional images and we cannot derive more than some exploratory conclusions. Due to this, we mainly focused on g'- and r'-band data.

We can observe several interesting behavior on the published surface brightness and color profiles. Although, on this sample it is not possible to derive statistically robust correlations, we find that the behavior of the surface brightness and color is connected to the surface brightness types of these galaxies.

In the Type II-CT galaxies in this sample (like NGC 0450 and NGC 0941) we find that the Type II behavior appears more pronounced in the u'-band. In NGC 0450 the u'-band surface brightness profile seems to have a sharp cut-off (see Figure 8), causing an enhanced “U-shape” on the (u'-g') color profile. Towards redder wavelengths the break feature seem to weaken and the “U-shape” flattens out (see Figures 8,9)

In BTP08 we obtained robust color profiles of Type I, Type II and Type III galaxies. For individual galaxies the (g'-r') color profiles reached a depth coinciding with ~ 25 mag arcsec $^{-2}$ on the r'-band surface brightness profiles. In the particular case of Type II galaxies, when we combined the information of many objects, we were able to derive a mean color profile down to ~ 27 mag arcsec $^{-2}$. This mean color profile was not just deeper but predicted the *general* behavior of Type II galaxies. Due to that analysis we found that this type of galaxies exhibit a “U-shape” on their (g'-r') color.

Now, using *Stripe82* data we got the opportunity to trace the color profiles down to fainter levels and confirm for instance the classical “U-shape” in case of individual galaxies. NGC 0450 and NGC 0941 are typical examples of this Type II behavior. Their g'-r' color profiles (see Figures 8, 9) follow nicely the “U-shape”, although, the gradient in the inner disk in NGC 0941 is much milder but with a prominent reddening beyond the break.

The same striking reddening can be observed beyond the break in NGC 7716 and UGC 02311. UGC 02081, despite of being classified as Type II based on its surface brightness profile, exhibits no reddening beyond the break. Actually, its flat color profile resembles that of what we found to be intrinsic in Type I galaxies. The color profile of NGC 1068 (Type I) is quite flat, it has some minor reddening around the turn-off radius presumably caused by the stellar halo light contribution. The $(r'-i')$ color profile of NGC 1068 does not reach the same depth, still, around the turn-off radius it shows the same slight reddening.

The color profile of NGC 1087 (see Figure 11) is puzzling. Based on its surface brightness profile we classified this galaxy as Type II*, associating the apparent break in the inner disk to the presence of a more concentrated star forming region. Meanwhile, the $g'-r'$ color profile exhibits a fairly deep “U-shape” around that break followed with a flattening around the radius where the stellar halo contribution starts to dominate the light. The overall shape of this color profile in BTP08 was associated with Type III galaxies.

Due to the low number of galaxies (~ 10) we did not obtain robust color profiles for Type I galaxies in BTP08, although, we have found the same flattened behavior for the mean color profile as along the disk in NGC 1068, the only Type I disk we could study in detail in this work. NGC 1068 has a rather dusty disk, so it is not unexpected that the mean color of the disk of NGC 1068 is rather red ($g'-r' \sim 0.6$).

In BTP08 we found a strong correlation for Type II galaxies between the color at the break with the absolute magnitude of the galaxy. If we compared the color at the break (see in Table 4) to the observed $(g'-r') = 0.47 \pm 0.02$ mag mean color of BTP08, we should expect that the main reason why the majority of the observed colors at the break are bluer than the BTP08 mean color is that these systems bear with less total stellar mass. It is indeed true that lower-mass systems such as NGC 0941 and UGC 02081 exhibit the bluest colors at the break in this sample. UGC 02311 also exhibits a blue color at the break, despite its high stellar mass. Although, in case of this Type II-ORL break one could expect enhanced star formation around the resonance zone. The presence of star forming rings around the outer Lindblad Resonance has been observed in many spirals (e.g. Buta & Crocker 1991; Buta 2002; Grouchy et al. 2010). The two peculiar Type II galaxies, NGC 1087 and NGC 7716, are similar in stellar mass to the mean value of BTP08, but only NGC 7716 has $(g'-r')$ color close to the BTP08 mean value.

5.3. Stellar surface mass density

As explained in Section 4.2.1, we obtained M/L ratio profiles from $(g'-r')$ colors. These profiles were converted into stellar surface mass density (Σ_*) profiles that serve as a proxy of the stellar mass distribution of our 7 galaxies. Though, when reaching the stellar halo the Bell & de Jong conversion formula (Bell & de Jong 2001) seems to break down, and the density basically becomes independent of the radial distance. This phenomena is quite evident in case of NGC 0450 and NGC 0941 (see e.g. Figures 8, 9). It is important to note that in these two galaxies we have observed extremely red colors in their

stellar halo. If these red colors are due to some extreme stellar populations (with a different IMF, for instance), the Bell & de Jong (2001) empirical formula cannot give valid predictions for the M/L , since it is largely based on the assumption of a Universal Salpeter-like IMF.

The Σ_* profiles of Type II galaxies do not follow the shape of the r' -band surface brightness profiles. Similarly to the findings of BTP08, the break diminishes on the stellar surface mass density profile. To quantify the ‘sharpness’ of the break on the Σ_* profile, we applied the same Bulge/Disk decomposition on the Σ_* profiles as for the surface brightness profiles. Not surprisingly, the inner-outer scale-lengths ratio takes a value of ~ 1 in NGC 0450, NGC 0941 and UGC 02311. In UGC 02081 the break, however, remains quite prominent, implying a different phenomena in this galaxy. (See last column on Figure 6).

In BTP08 we found that at Type II galaxies, the mean stellar mass density at the break radius is $\sim 10 M_\odot \text{ pc}^{-2}$. Taking into account that at the break positions of NGC 1087 and NGC 7716 the stellar surface mass density is much higher than this value ($\sim 99 M_\odot \text{ pc}^{-2}$ and $\sim 31 M_\odot \text{ pc}^{-2}$, respectively), not classifying these galaxies as Type II-CT seems justified. On the Σ_* profile of UGC 02081 we observe quite an irregular cut-off, that seems to be a real mass drop after the break radius. Also, the Σ_* has a low value at the break radius ($\Sigma_{*,br} = 1.7 M_\odot \text{ pc}^{-2}$), this value is much lower than the average value found in BTP08.

5.4. Stellar populations in the stellar halos

The observed $(g'-r')$ colors for our stellar halos cover a large range from ~ 0.4 to ~ 1.2 . This is a rather unexpected variety of colors and stellar populations contained within the stellar halos, independently of the total stellar mass of the host galaxy.

In order to learn about the nature of the stellar populations behind these observed colors, we compared them to stellar population model predictions (Vazdekis et al. 2010). As it is already explained in Section 4.3, Figure 4 is only a crude way to visualize what the stellar population content of these stellar halos might be. We chose two typical stellar halos to do this analysis, the red stellar halo of NGC 1068 ($(g' - r') \sim 0.55$) and the extremely red stellar halo of NGC 0941 ($(g' - r') \sim 0.95$). It is important to note, that the observed stellar halo colors are redder than that of the disk or even the bulge (with the exception of NGC 1068, which has a very dusty disk, hence the stellar halo appears to be bluer than the disk).

It is relatively obvious that with the error bars of our measurements neither metallicity, nor age can really be constrained. However, by assuming that the stellar halo properties of our galaxies are similar to the ones in our neighborhood, we can make some further but tentative constraints based on observations of nearby galaxies. For instance, it is widely accepted that the Milky Way stellar halo is dominated by a metal-poor population ($[Fe/H] \lesssim -1.5$) (e.g. Ryan & Norris 1991; Carollo et al. 2007; Ivezić et al. 2008, and references therein). In other nearby galaxies, like M31 (Ferguson et al. 2002; Chapman et al. 2006; Ibata et al. 2007), M33 (Davidge 2003; McConnachie et al. 2006; Barker et al. 2007; Grossi et al. 2011), or NGC 2403

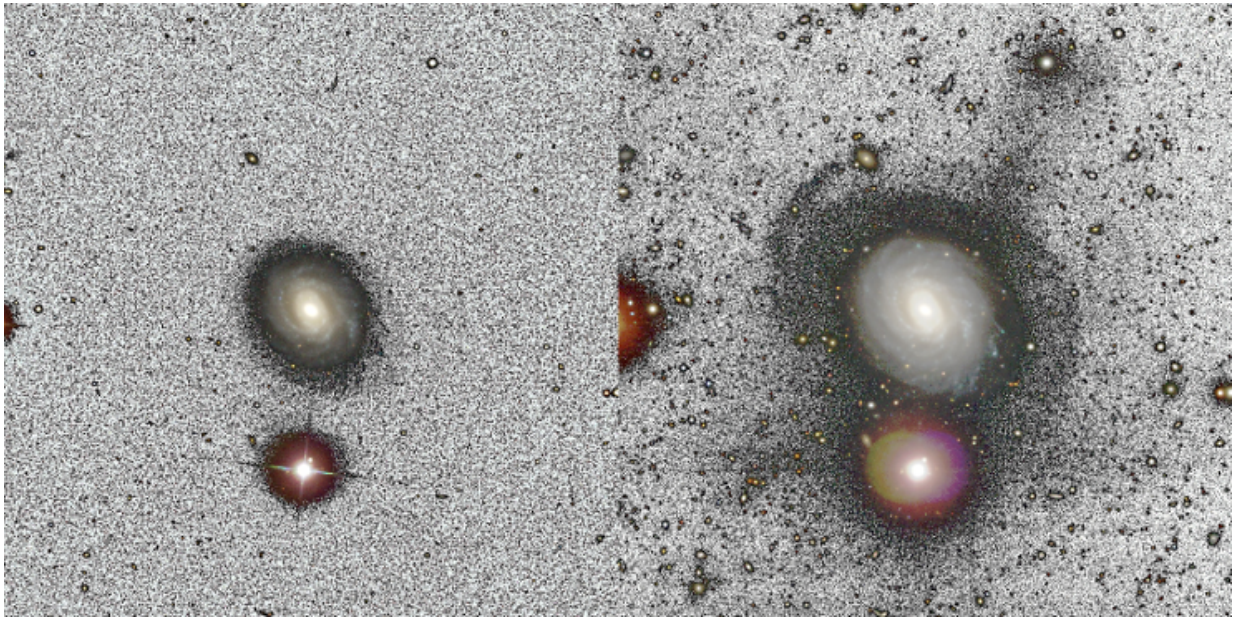


Figure 7. *Left image:* NGC7716 in SDSS r' -band (single exposure). The limiting surface brightness of this image is ~ 27 mag arcsec $^{-2}$, which corresponds to 3σ of the skynoise. The skynoise (similarly to PT06) is the resistant mean of the skyvalues measured on the pixels in an aperture surrounding the galaxy. *Right image:* *Stripe82* coaddition of NGC7716 with clearly visible tidal streams likely originating from two satellites. The surface brightness of the streams is ~ 27 mag arcsec $^{-2}$ in r' -band.

(Davidge 2003; Barker et al. 2012), the stellar halos consist of predominantly old and metal-poor ($[Fe/H] \sim -0.7$ – -1.5) stellar populations.

It is interesting to note that SSP models produced with conventional Kroupa IMF ($\alpha = 1.3$) predict that the stellar halo color observed in NGC 0941 would imply a stellar halo that is fairly metal-rich and old. This is at odds with the measurements in nearby galaxies. By changing the IMF, though, it is possible to look for solutions that would attribute the red colors to metal-poor stellar populations. It has already been discussed in the literature (e.g. Zackrisson et al. 2006, and references therein) that a bottom-heavy IMF could be responsible for such red colors. Following this idea, we applied a bottom-heavy IMF with a slope of $\alpha = 3.3$ to compute our model ($g'-r'$) colors. These models indeed yield possible solutions of $\tau \gtrsim 4$ Gyr old and $[Fe/H] \lesssim -1.5$. In case of NGC 1068, this IMF would imply a young stellar halo (younger than in case of Kroupa IMF) with any metallicity possible.

6. DISCUSSION

Using deep SDSS *Stripe82* data we observed the stellar content of 7 late-type galaxies down to $\mu_{r'} \sim 30$ mag arcsec $^{-2}$. This is roughly a stellar surface mass density of $\sim 0.1 M_{\odot} \text{ pc}^{-2}$, allowing us to study the stellar halo component of these galaxies.

At present, Stellar halos are best studied by resolved star technique, and there have been only a few attempts to study stellar halos by integrated photometry (e.g. Jablonka et al. 2010). However, to explore galaxies beyond our neighborhood, integrated photometry is needed. Resolved star technique provides ample information on stellar halos: the surface brightness of stellar halos in external galaxies, and how their contribution affects the surface brightness profile. From recent observations of nearby galaxies such as M31 or NGC2403 we know the structure of the disks and stellar halos of these galaxies in unprecedented detail (e.e.

Courteau et al. 2011; Barker et al. 2012).

Tha galaxies in our sample are similar in stellar mass and in Hubble-type to many of these well studied systems. Although, stochastic variations in the evolutionary path of these individual galaxies could cause striking differences as to how the structural properties of the different substructures vary from galaxy to galaxy on the same mass scale. Still, Courteau et al. (2011) argued that one should expect to encounter the signatures of stellar halos in surveys that reach below the depth of $\mu_{r'} \sim 27.5$ mag arcsec $^{-2}$. Using SDSS data PT06 extracted surface brightness profiles down to a similar depth, but the questioned remained: *What is the real extent of disks? Does the exponential disk continue down to lower surface densities as predicted by some models?* In many cases the structure of the outer disk does not change right below 27 mag arcsec $^{-2}$. The outer disk indeed follows an exponential surface brightness profile down to the level where there is a smooth continuation into the region where the stellar halo light dominates over the disk light (causing the upturns discussed beforehand at the level of $\mu_{r'} \sim 28$ mag arcsec $^{-2}$).

Due to this mixture of components, we are unable to determine the real extent of the disks. It would seem that this disk-stellar halo light conspiracy is due to the observing geometry. In face-on geometry we cannot decouple the light of the stellar halo from that of the disk. Because when we study the surface brightness distribution of these two components, we rely on the superimposed two dimensional projection of both the stellar halo and the disk. The only way to explore further the disk light would be in edge-on projection. In edge-on projection by integrating the light of the galaxy along the line-of-sight of the disk, the contrast between the disk and the stellar halo is enhanced, allowing us to explore around ~ 2 mag deeper the disk component.

Our deep surface brightness profiles has modified our view on how surface brightness profiles should be classi-

fied. By making use of, for instance, high quality color profiles it was possible to rethink the previous classification scheme, especially in relation to Type III profiles.

6.1. On the nature of Type III profiles

The nature of Type III profiles since their discovery (Erwin et al. 2005) proved to be contradictory. Any comprehensive picture regarding the nature of Type III profiles needs to explain: why we observe two sub-class of Type III profiles (with disk like or spheroid like isophotes in the outskirts), the origin of the peculiar color profile of Type III galaxies, and why the statistics of Type III profiles decreases towards later Hubble-types.

The fraction of Type III profiles becomes larger in early-type spirals (PT06, Erwin et al. 2008). Consequently, as the prominence of the bulge increases with the same trend, one could hazard that Type III profiles are nothing else but the bulge component emerging above the disk component on the surface brightness profiles. This would also explain the roundish isophotes that many of these Type III galaxies present in their outer regions. Indeed, being motivated by this idea, Maltby et al. (2012) studied the connection between the bulges and Type III profiles in a sample of intermediate redshift galaxies. They found that especially in early-type disk galaxies Type III profiles are caused by the aforementioned bulge emergence, but they could not refute the idea that in many cases, however, it remains a pure disk phenomenon. *What is the origin of Type III profiles in late-type galaxies where the bulge component is rather small to be held responsible for such phenomena, and where the light of the outer region clearly follows disk isophotes?*

In our sample, we have found that the contribution of the stellar halo light on the surface brightness profiles causes a similar upturn as on ‘classical’ Type III profiles. In case of NGC 1087 this contribution is so high that it starts to affect the surface brightness profile at a higher surface brightness level. Due to this, this galaxy previously was classified as Type III (PT06; BTP08). It is natural to ask whether it is a unique behavior of this galaxy or a general rule that would mean that we should find many examples once looked carefully. Interestingly, M81 (a twin of NGC 1087 with its absolute magnitude of $M_B = -20.7$ mag) is also a system with an unusually bright halo component, though Barker et al. (2009) also consider the possibility that the extended bright component in M81 belongs to a disk feature (e.g. thick disk). Regardless of this, the light fraction of this component compared to the total luminosity in both galaxies is $\sim 10\%$. In NGC 7716 the stellar halo is similarly bright, moreover in this galaxy the misaligned outer disk, that causes a sharp Type III break, can be associated with clear interaction. The tidal stream we identified around this galaxy is clearly connected to this misaligned outer disk.

NGC 1087 and NGC 7716 have a central star forming region in their inner disk that causes a high surface brightness break on their surface brightness profile that we indicated with an “asterix Type II” profile (distinguishing from the usual Type II classification because this break is *not* the phenomena we usually associate with the *end* of the spiral arms). We can assume that the enhanced star formation in the inner disk is trig-

gered by the recent interaction that has either supplied the material necessary to form stars or redistributed the gas already settled inside the disk. If this scenario is plausible, we can immediately understand why we observe such a peculiar shape of the Type III color profiles. As it was already shown in BTP08 (see their Figure 1) Type III galaxies seem to retain the “U-shape” at shorter galactocentric radii, with a red “plateau” residing at the Type III break followed by a blueing towards the outskirts. It is remarkable that NGC 1087 retains this shape on its ($g'-r'$) color profile, at the Type II* break with the bluest color and at the Type III break with a red “plateau”. NGC 7716 also exhibits the bluest color at the position of the Type II* break.

Combining all the information from the surface brightness and color profiles, we propose the following unified picture of Type III (late-type) galaxies: Type III profiles are not an individual class of galaxies but rather, Type I or Type II galaxies with a stellar halo. The surface brightness level at which the stellar halo contributes depends on the recent evolutionary history (and stellar mass) of the galaxy. Galaxies are transformed by (recent) interaction. The infalling new material enriches the stellar halo, can add extra material to the disk and trigger star formation leading to a Type II+III mixed profile. Meanwhile, a more quiescent history means a less developed stellar halo, that would explain the existence of pure Type III profiles (see the published profiles of PT06 and Erwin et al. 2008).

Due to this, in any flux limited survey that cannot probe the surface brightness levels of quiescent stellar halos, the “Type III profiles” would remain unobserved. This also would explain the low number of Type II+III profiles in the PT06 sample ($\sim 5\%$), that necessarily comes from the combined effect of a high surface brightness Type II break and a bright stellar halo/tidal stream on the surface brightness profile. Type II+III late-type galaxies would be late disks ‘caught’ during a merger event.

6.2. Further clues on outer-disk formation

What clues can we deduce from the results of this paper in relation to the formation of breaks in the surface brightness profile of disk galaxies? Can these deep surface brightness, color and stellar surface mass density profiles constrain the formation of these individual systems by making use of the predictions of current models?

The *formation of Type II breaks* is an issue that has been addressed for a long time and with a renewed vigor during the past couple of years. As we have already referred in Section 1, the new rendition of models incorporate the effect of a star formation threshold and the redistribution of stars by secular processes (migration) as key ingredient to match the observational evidence in disk galaxies (Roškar et al. 2008; Sánchez-Blázquez et al. 2009; Martínez-Serrano et al. 2009). These models have remarkably similar predictions of an existing minimum on the age profile occurring right at the break position followed by a likely ageing towards the outskirts. This was the natural consequence of the net migration of stars.

The ageing in the outskirts in case of an absent metallicity gradient can be seen as reddening on the color profiles. The Type II “U-shape” ($g'-r'$) color profiles for this reason are in qualitative agreement with the predictions

of Roškar et al. (2008); Sánchez-Blázquez et al. (2009); Martínez-Serrano et al. (2009). A disagreement between the observational and theoretical results of BTP08 and Roškar et al. (2008) was that BTP08 proposed the (*near*) *absence of the break* on the stellar surface mass density profile.

In BTP08 we could not show this phenomena on the individual galaxy profiles due to the insufficient depth of the SDSS data that prevented us to trace the ($g'-r'$) color or the Σ_* profiles well beyond the break radius. Although, based on the robust mean Σ_* profiles, in BTP08 we claimed that the break on the surface brightness profile signifies a radial change in the key ingredients of the stellar population rather than being caused by a mass drop beyond the break radius. Based on the results revealed in this paper, we find strong indication that there is no mass drop beyond the break radius. We demonstrated on Figure 6 that the inner-out disk scale-lengths ratio obtained from the stellar surface mass density drops to ~ 1 .

The inner-outer scale-lengths ratio strongly depends on the observing wavelength, as well (see Figure 6). The prominence of the break decreases from u'-band towards redder filters, in a way that surface brightness profile of the inner disk is the *flattest* in the u'-band (in Bakos & Trujillo 2010 we observed the same trend on a few selected 'grand-design' spirals.) Consequently, the inner disk *must be* dominated by recently formed, young stars that are distributed homogeneously along the inner disk, meanwhile old stars can be found everywhere in the disk. Remarkably, our *observations* are in qualitative agreement with the predictions of Sánchez-Blázquez et al. (2009) who also showed that the break becomes more pronounced in bluer wavebands. It is however interesting to note, that they find that migration is not the main mechanism producing this particular shape of the age profile. The same trend is observed with and without migration. When looking for explanation for the absence of breaks in the stellar surface mass density profile, however, stellar migration is a key process that weakens the intensity of the break in the Σ_* profile. *In situ* star formation in the outer disk cannot produce sufficient amount of stars to conform the lack of or weak breaks. Based on broad-band colors it seems that migration and *in situ* star formation are both relevant.

On the other hand, we need to stress the importance of the discovery of galaxies like UGC 02081 that based on their surface brightness profile are classified as Type II but do not exhibit the "U-shape", moreover retain a significant mass drop right after the break radius. By finding that the Σ_* at the break is at much lower stellar surface mass density ($\sim 1M_\odot pc^{-2}$) than the observed mean value ($\sim 10M_\odot pc^{-2}$), we think we need to treat them as distinct sub-class of Type II profiles. The low Σ_* value at the break and the sharp behavior of the Σ_* profile of UGC 02081 at its outskirts resembles more of the traditional picture of truncations (truncations could be imagined as the 'edge' of disks) proposed by van der Kruit (1979). UGC 02081 could be one of the few moderately inclined galaxies where a real truncation is observed.

Finally, in this paper, we propose that Type III profiles are in fact signatures of the stellar halo (or tidal streams). For this reason, the *formation of Type III breaks* seems

to be a natural consequence of the current cosmological paradigm. Satellites are expected to interact with their host galaxy. Their orbital parameters (angular momentum, for instance) will decide how their interaction changes the morphology of the host galaxy, whether the remnants build the stellar halo or rather settle in the disk (Younger et al. 2007, 2008; Kazantzidis et al. 2008). We find that in NGC 7716 a disk Type III morphology can be associated to a misaligned outer disk that is in connection with a tidal stream of an unknown progenitor. The jet-like structure more or less perpendicular to the disk could be part of another loop. These tidal features are well-known around several late-type disks. Just recently, Wang et al. (2012) investigated the possibility that loops in NGC 5907 are formed after a major merger event, challenging the dominance of minor merger scenarios to form such substructures.

6.3. Stellar halos beyond the local volume

We observed the presence of stellar halos in 7 spiral galaxies. The signature of the stellar halo is a well-defined upturn followed by a flattening on the deep r' -band surface brightness profiles, that can be observed in the other two deep, g' - and i' -bands.

Although, the number of systems we can compare to is limited, we can find solid examples of stellar halos observed by 'resolved star' technique in nearby galaxies. If we compare the surface brightness profiles of our galaxies to star-count profiles of Local Group and other nearby galaxies within the next ~ 15 Mpc, we find that those profiles exhibit the same behavior at similar distances and surface brightness levels. In our galaxies the stellar halo starts to dominate as far as $\sim 10 - 40$ kpc, farther in more luminous hosts (see Table 5). Courteau et al. (2011) reported that in M31 the stellar halo starts to dominate at ~ 9 kpc over the light of the disk component. NGC 2403 ($M_B = -19.44$ mag), a far more isolated system than M31 and analogous to NGC 0941, also exhibit an extended light component that becomes the dominant feature of the stellar count profile at ~ 18 kpc radius (Barker et al. 2012).

The light fraction of the stellar halos in our galaxies fall in the range of 1 – 5 %. These are typical values found in nearby galaxies, the stellar halo light fractions observed in the Milky Way (Carollo et al. 2010), M31 (Courteau et al. 2011) or in NGC 2403 (Barker et al. 2012) are of the same order we find in our galaxies. The light fraction found in an asymmetric substructure surrounding M33 is $\sim 1\%$ (McConnachie et al. 2010).

According to the findings of Purcell et al. (2007) that investigated the formation of stellar halos through merger-history, the light fraction in stellar halos depends on the total stellar mass of the system and the accretion history of the galaxy, hence on the mass of the dark matter halo. Although, the observed stellar mass (or absolute magnitude) range of our galaxies is of the order of 4 magnitudes, we do not find evidence of the stellar halo light increasing with the host galaxy mass. This might occur if due to the relatively low number of galaxies observed in this sample, the variations in the accretion history of these galaxies *smears* out the correlation expected to be seen with the total galaxy mass. We do find that in the two systems where we discovered the signs of recent interaction the stellar halo light fraction

is systematically higher ($\sim 10\%$).

Other cosmological simulations also emphasize the possibility of a dual origin of stellar halos. In this scenario, stellar halos should contain stars that were formed *in situ* and stars that were accreted from lower mass satellites (e.g. Zolotov et al. 2009; Font et al. 2011). Consequently, more massive galaxies are expected to have more metal rich stellar halos. On the observational side there are contradictory findings so far. Mouhcine et al. (2005) suggested that the metallicity of stellar halos in more massive systems is indeed higher, however, Ferguson et al. (2007) showed that the observed photometric metallicities can be largely biased that can be overcome by kinematically selecting the halo star population. As a results of such a careful treatment of halo stars, they found no evidence of correlation between stellar halo metallicity and host galaxy luminosity.

The stellar halo colors we find in our galaxies show no correlation with the host galaxy mass (absolute magnitude) either. We observed a range of different halo colors from red to extremely red, but we have found both 'blue' and red colors in lower-mass systems, namely in NGC 0941 (See Figure 9) and UGC 02081 (See Figure 9). If not the host galaxy mass then what drives the color distribution of these stellar halos? Do galaxies evolving in isolation have redder colors? Is there any reason to believe that a variant IMF is responsible for the observed colors? Or is there a large population of stars formed *in situ* that could account for the presence of an extremely old but metal-poor population? These are questions that so far remain without answer.

We used the latest MILES SSP models to give crude constraints on the stellar populations embedded within these stellar halos. It is evident that resolved star technique yields more accurate stellar population properties, like metallicities. Broad-band colors are affected by the age-metallicity degeneracy, so it is not possible to ascertain the stellar populations dominating the stellar halos of our galaxies. The typical stellar halo colors seem be in agreement with the ages and metallicities of nearby galaxies ($\tau \sim 5$ Gyr and $[\text{Fe}/\text{H}] \sim -1.5$). But extreme red halo colors cannot be reconciled with such populations or with the current cosmological paradigm. We find compelling evidence that these extreme red colors may indicate a varying IMF. A bottom-heavy IMF could be the key agent in producing such red populations. Such solution to the red halo phenomenon has also been suggested by several authors (e.g. Zackrisson et al. 2006, 2012).

7. CONCLUSIONS

1. The light contribution from the stellar halo in the surface brightness profiles of spiral galaxies causes Type III profiles: the surface brightness level at which the surface brightness profile starts to deviate from the exponential profile of the disk depends on the brightness of the stellar halo. The brighter the stellar halo, the brighter the Type III "break". Disky Type III profiles are caused by tidal streams, that also belong to the stellar halo. These effects could be responsible for previous classification of surface brightness profiles of late-type galaxies as Type III.
2. High surface brightness disk breaks ($\mu_{r'} \sim 22$ mag

arcsec^{-2}) could be an indication of recent interaction. The new infalling material (gas) settles into the center of the disk and triggers star formation in the inner disk.

3. The stellar halos of quiescent systems contribute less to the total light of the galaxy.
4. Stellar halos show a large range of $(g' - r')$ colors. Some of them, are extremely red ($g' - r' > 1$), allowing for the possibility of bottom-heavy IMFs to explain the red halo colors.

8. SUMMARY

In this paper we have explored the structure and stellar population content of 7 late-type spirals using re-stacked deep data from SDSS *Stripe82*. This data typically reaches ~ 2 magnitudes deeper in the 5 bands than regular SDSS data. In the r' -band the quality of the data made it possible to reach a surface brightness level of ~ 30 mag arcsec^{-2} .

Using the deep r' -band profiles we classified our galaxies into the three classical types (Type I, Type II, and Type III). All surface brightness profiles change their behavior around ~ 28 mag arcsec^{-2} . A flattening is observed on all profiles that we believe to be the signature of stellar halos.

These faint levels composed of the outer stellar disk and stellar halo beforehand were only reached by techniques that involve resolving stars in these regions or stacking many individual objects. The resolved star technique, although is very powerful, is limited to galaxies that are in the reach of the resolving power of current telescopes. Studies of nearby galaxies like M31, M33, NGC2403 showed that the faint outer regions consist of an ample stellar content with many substructures present in them. We have found different stellar halo color implying very distinct stellar halo populations among our galaxies. We find compelling evidence that there exist extreme red colors halo colors that can be explained by stellar populations that are formed from a bottom-heavy IMF. Meanwhile, less red colors we find in other stellar halos could imply metal-poor ($[\text{Fe}/\text{H}] \sim -1.5$) and old ($\tau \gtrsim 5$ Gyr) stellar populations consistent with the stellar populations found in more nearby galaxies. The light fraction in the stellar halos of our galaxies is 1–5%, but in galaxies where recent interaction occurred, it can reach 10%. In NGC 7716 we have discovered the presence of a giant stellar stream, and a ~ -14 r' -mag satellite in the vicinity of NGC 1068.

9. ACKNOWLEDGEMENT

This work has been supported by the Programa Nacional de Astronomía y Astrofísica of the Spanish Ministry of Science and Innovation under grant AYA2010-21322-C03-02. JB would like thank the following people who in many ways contributed to this paper: Alexandre Vazdekis, Jesús Falcón-Barroso, Peter Erwin, Daniella Calzetti, John Kormendy, James Binney, Reynier Peletier, Stephan Courteau and Ignacio Ferreras.

REFERENCES

- Abazajian, K. N., Adelman-McCarthy, J. K., Agüeros, M. A., et al. 2009, *ApJS*, 182, 543

- Andredakis, Y. C., Peletier, R. F., & Balcells, M. 1995, *MNRAS*, 275, 874
- Annis, J., Soares-Santos, M., Strauss, M. A., et al. 2011, *ArXiv e-prints*
- Azzollini, R., Trujillo, I., & Beckman, J. E. 2008a, *ApJ*, 679, L69
- . 2008b, *ApJ*, 684, 1026
- Bakos, J., & Trujillo, I. 2010, in *American Institute of Physics Conference Series*, Vol. 1240, American Institute of Physics Conference Series, ed. V. P. Debattista & C. C. Popescu, 287–288
- Bakos, J., Trujillo, I., & Pohlen, M. 2008, *ApJ*, 683, L103, (BTP08)
- Barker, M. K., Ferguson, A. M. N., Irwin, M., Arimoto, N., & Jablonka, P. 2009, *AJ*, 138, 1469
- Barker, M. K., Ferguson, A. M. N., Irwin, M. J., Arimoto, N., & Jablonka, P. 2012, *MNRAS*, 419, 1489
- Barker, M. K., Sarajedini, A., Geisler, D., Harding, P., & Schommer, R. 2007, *AJ*, 133, 1125
- Bell, E. F., & de Jong, R. S. 2001, *ApJ*, 550, 212
- Bell, E. F., McIntosh, D. H., Katz, N., & Weinberg, M. D. 2003, *ApJS*, 149, 289
- Bell, E. F., Zucker, D. B., Belokurov, V., et al. 2008, *ApJ*, 680, 295
- Belokurov, V., Evans, N. W., Irwin, M. J., et al. 2007, *ApJ*, 658, 337
- Bergvall, N., Zackrisson, E., & Caldwell, B. 2010, *MNRAS*, 405, 2697
- Bertin, E. 2010a, *PSFex v3.9 User's guide*
- . 2010b, *SWarp v2.20 User's guide*
- Bertin, E., & Arnouts, S. 1996, *A&AS*, 117, 393
- Brook, C. B., Kawata, D., Gibson, B. K., & Freeman, K. C. 2004, *ApJ*, 612, 894
- Bullock, J. S., & Johnston, K. V. 2005, *ApJ*, 635, 931
- Buta, R. 2002, in *Astronomical Society of the Pacific Conference Series*, Vol. 275, *Disks of Galaxies: Kinematics, Dynamics and Perturbations*, ed. E. Athanassoula, A. Bosma, & R. Mújica, 185–192
- Buta, R., & Crocker, D. A. 1991, *AJ*, 102, 1715
- Carollo, D., Beers, T. C., Lee, Y. S., et al. 2007, *Nature*, 450, 1020
- Carollo, D., Beers, T. C., Chiba, M., et al. 2010, *ApJ*, 712, 692
- Chapman, S. C., Ibata, R., Lewis, G. F., et al. 2006, *ApJ*, 653, 255
- Cooper, A. P., Cole, S., Frenk, C. S., et al. 2010, *MNRAS*, 406, 744
- Courteau, S., Widrow, L. M., McDonald, M., et al. 2011, *ApJ*, 739, 20
- Davidge, T. J. 2003, *AJ*, 125, 3046
- de Jong, R. S. 1996, *A&A*, 313, 45
- . 2008, *MNRAS*, 388, 1521
- de Vaucouleurs, G. 1958, *ApJ*, 128, 465
- Erwin, P. 2004, *A&A*, 415, 941
- Erwin, P., Beckman, J. E., & Pohlen, M. 2005, *ApJ*, 626, L81
- Erwin, P., Pohlen, M., & Beckman, J. E. 2008, *AJ*, 135, 20
- Ferguson, A., Irwin, M., Chapman, S., et al. 2007, *Island Universes - Structure and Evolution of Disk Galaxies*, ed. de Jong, R. S. (Springer, Dordrecht), 239
- Ferguson, A. M. N., Irwin, M. J., Ibata, R. A., Lewis, G. F., & Tanvir, N. R. 2002, *AJ*, 124, 1452
- Font, A. S., McCarthy, I. G., Crain, R. A., et al. 2011, *MNRAS*, 416, 2802
- Freeman, K. C. 1970, *ApJ*, 160, 811
- Gilmore, G., Wyse, R. F. G., & Norris, J. E. 2002, *ApJ*, 574, L39
- Graham, A. W. 2001, *AJ*, 121, 820
- Grossi, M., Hwang, N., Corbelli, E., et al. 2011, *A&A*, 533, A91
- Grouchy, R. D., Buta, R. J., Salo, H., & Laurikainen, E. 2010, *AJ*, 139, 2465
- Ibata, R., Martin, N. F., Irwin, M., et al. 2007, *ApJ*, 671, 1591
- Ibata, R. A., Gilmore, G., & Irwin, M. J. 1994, *Nature*, 370, 194
- Ivezić, Ž., Sesar, B., Jurić, M., et al. 2008, *ApJ*, 684, 287
- Jablonka, P., Tafelmeyer, M., Courbin, F., & Ferguson, A. M. N. 2010, *A&A*, 513, A78
- Jurić, M., Ivezić, Ž., Brooks, A., et al. 2008, *ApJ*, 673, 864
- Kazantzidis, S., Bullock, J. S., Zentner, A. R., Kravtsov, A. V., & Moustakas, L. A. 2008, *ApJ*, 688, 254
- Kennicutt, Jr., R. C. 1989, *ApJ*, 344, 685
- Khachikian, E. Y., & Weedman, D. W. 1974, *ApJ*, 192, 581
- Kormendy, J., & Kennicutt, Jr., R. C. 2004, *ARA&A*, 42, 603
- Kroupa, P. 2001, *MNRAS*, 322, 231
- Lequeux, J., Combes, F., Dantel-Fort, M., et al. 1998, *A&A*, 334, L9
- MacArthur, L. A., Courteau, S., & Holtzman, J. A. 2003, *ApJ*, 582, 689
- Majewski, S. R., Siegel, M. H., Kunkel, W. E., et al. 1999, *AJ*, 118, 1709
- Maltby, D. T., Gray, M. E., Aragón-Salamanca, A., et al. 2012, *MNRAS*, 419, 669
- Markwardt, C. B. 2009, in *Astronomical Society of the Pacific Conference Series*, Vol. 411, *Astronomical Data Analysis Software and Systems XVIII*, ed. D. A. Bohlender, D. Durand, & P. Dowler, 251–+
- Martínez-Delgado, D., Peñarrubia, J., Gabany, R. J., et al. 2008, *ApJ*, 689, 184
- Martínez-Delgado, D., Pohlen, M., Gabany, R. J., et al. 2009, *ApJ*, 692, 955
- Martínez-Serrano, F. J., Serna, A., Doménech-Moral, M., & Domínguez-Tenreiro, R. 2009, *ApJ*, 705, L133
- McConnachie, A. W., Chapman, S. C., Ibata, R. A., et al. 2006, *ApJ*, 647, L25
- McConnachie, A. W., Ferguson, A. M. N., Irwin, M. J., et al. 2010, *ApJ*, 723, 1038
- McConnachie, A. W., Irwin, M. J., Ibata, R. A., et al. 2009, *Nature*, 461, 66
- Mouhcine, M., Ferguson, H. C., Rich, R. M., Brown, T. M., & Smith, T. E. 2005, *ApJ*, 633, 810
- Mouhcine, M., Ibata, R., & Rejkuba, M. 2010, *ApJ*, 714, L12
- Newberg, H. J., Yanny, B., Rockosi, C., et al. 2002, *ApJ*, 569, 245
- Patterson, F. S. 1940, *Harvard College Observatory Bulletin*, 914, 9
- Pérez, I. 2004, *A&A*, 427, L17
- Pohlen, M., Dettmar, R.-J., Lütticke, R., & Aronica, G. 2002, *A&A*, 392, 807
- Pohlen, M., & Trujillo, I. 2006, *A&A*, 454, 759, (PT06)
- Purcell, C. W., Bullock, J. S., & Zentner, A. R. 2007, *ApJ*, 666, 20
- Rejkuba, M., Mouhcine, M., & Ibata, R. 2009, *MNRAS*, 396, 1231
- Roškar, R., Debattista, V. P., Stinson, G. S., et al. 2008, *ApJ*, 675, L65
- Ryan, S. G., & Norris, J. E. 1991, *AJ*, 101, 1835
- Sánchez-Blázquez, P., Courty, S., Gibson, B. K., & Brook, C. B. 2009, *MNRAS*, 398, 591
- Schaye, J. 2004, *ApJ*, 609, 667
- Schinnerer, E., Eckart, A., Tacconi, L. J., Genzel, R., & Downes, D. 2000, *ApJ*, 533, 850
- Sérsic, J. L. 1968, *Atlas de galaxies australes (Cordoba, Argentina: Observatorio Astronomico)*
- Tanaka, M., Chiba, M., Komiyama, Y., et al. 2010, *ApJ*, 708, 1168
- Trujillo, I., Asensio Ramos, A., Rubiño-Martín, J. A., et al. 2002, *MNRAS*, 333, 510
- Trujillo, I., Graham, A. W., & Caon, N. 2001, *MNRAS*, 326, 869
- Trujillo, I., Martínez-Valpuesta, I., Martínez-Delgado, D., et al. 2009, *ApJ*, 704, 618
- Trujillo, I., & Pohlen, M. 2005, *ApJ*, 630, L17
- van der Kruit, P. C. 1979, *A&AS*, 38, 15
- Vazdekis, A., Sánchez-Blázquez, P., Falcón-Barroso, J., et al. 2010, *MNRAS*, 404, 1639
- Wang, J., Hammer, F., Athanassoula, E., et al. 2012, *A&A*, 538, A121
- Younger, J. D., Besla, G., Cox, T. J., et al. 2008, *ApJ*, 676, L21
- Younger, J. D., Cox, T. J., Seth, A. C., & Hernquist, L. 2007, *ApJ*, 670, 269
- Zackrisson, E., Bergvall, N., Östlin, G., Micheva, G., & Leksell, M. 2006, *ApJ*, 650, 812
- Zackrisson, E., de Jong, R. S., & Micheva, G. 2012, *MNRAS*, 2314
- Zaritsky, D., Smith, R., Frenk, C., & White, S. D. M. 1993, *ApJ*, 405, 464
- Zibetti, S., & Ferguson, A. M. N. 2004, *MNRAS*, 352, L6
- Zibetti, S., White, S. D. M., & Brinkmann, J. 2004, *MNRAS*, 347, 556
- Zolotov, A., Willman, B., Brooks, A. M., et al. 2009, *ApJ*, 702, 1058

APPENDIX

A. GALAXY ATLAS

In this section we publish the surface brightness, color, stellar surface mass density profiles of the 7 spiral galaxies of our sample. These figures contain a RGB color composite stamp created from the deep g'-, r'-, and i'-band stacks. These stacks were created using STIFF. In order to help the identification of low surface brightness features by naked eye, we inverted the black background later on. In some cases we also used “unsharp masking” to enhance these features. (All images have the same orientation with North displayed upwards and with East to left.)

The top right panel contains the r'-band profile of our galaxies. The plot contains the observed profiles, and the 1σ (blue shade) and 3σ (purple shade) error regions. We drew a blue dashed line to indicate the 3σ noise-level of the sky, the radius where the profile reaches this level is indicated with the blue ellipse on the color image.

The r'-band profile served as the basis for decomposing the different structures building up the galaxies, like bulge (*green dots*), disk (*black dotted-dashed lines*), and stellar halo (*yellow dots*) components. The decomposition is explained in detail in Section 4.1.3. The final composite profile is drawn over the observed profile by *red open circles*. The region where the stellar halo contributes to the total light of the galaxy with more than 50% is indicated by the green shade. If the surface brightness profile of the galaxy exhibits a break, it is shown by a vertical red dashed line on the profile, and with a red ellipse on the color image.

The middle left hand panel shows the (g'-r') color profile using scarcely placed bins. For the stellar halo we derived one single color.

The middle right hand panel shows the Σ_* profile (for further information see Section 4.2.3).

The bottom right and left panels contain the surface brightness profiles and color profiles in all available SDSS filters obtained from the *Stripe82* imaging. The surface brightness and color profiles are color coded as indicated on the figures.

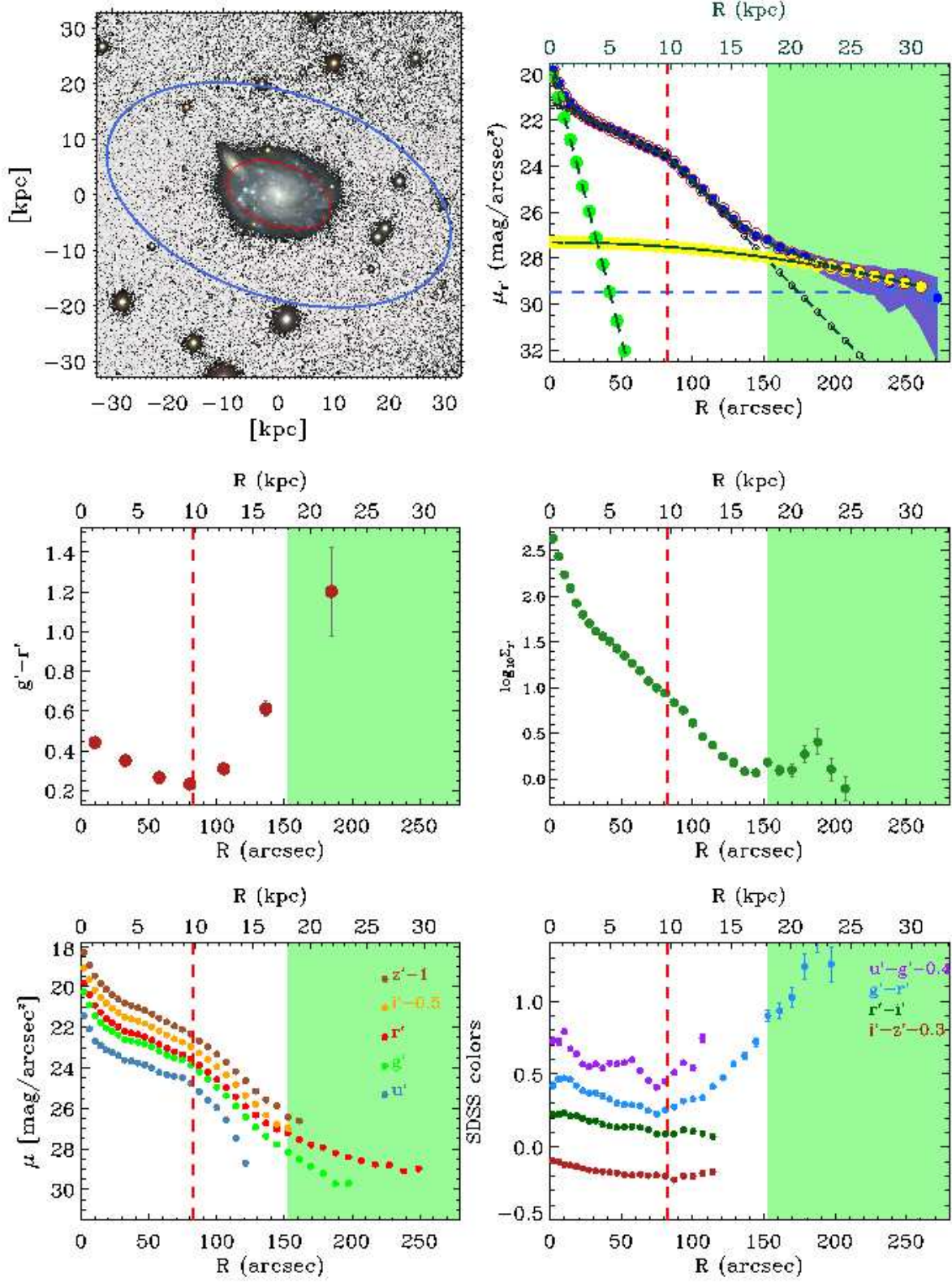


Figure 8. NGC 0450: It is a moderately inclined spiral galaxy with a background galaxy (UGC00807) superimposed. It has been classified by PT06 as a Type II-CT.

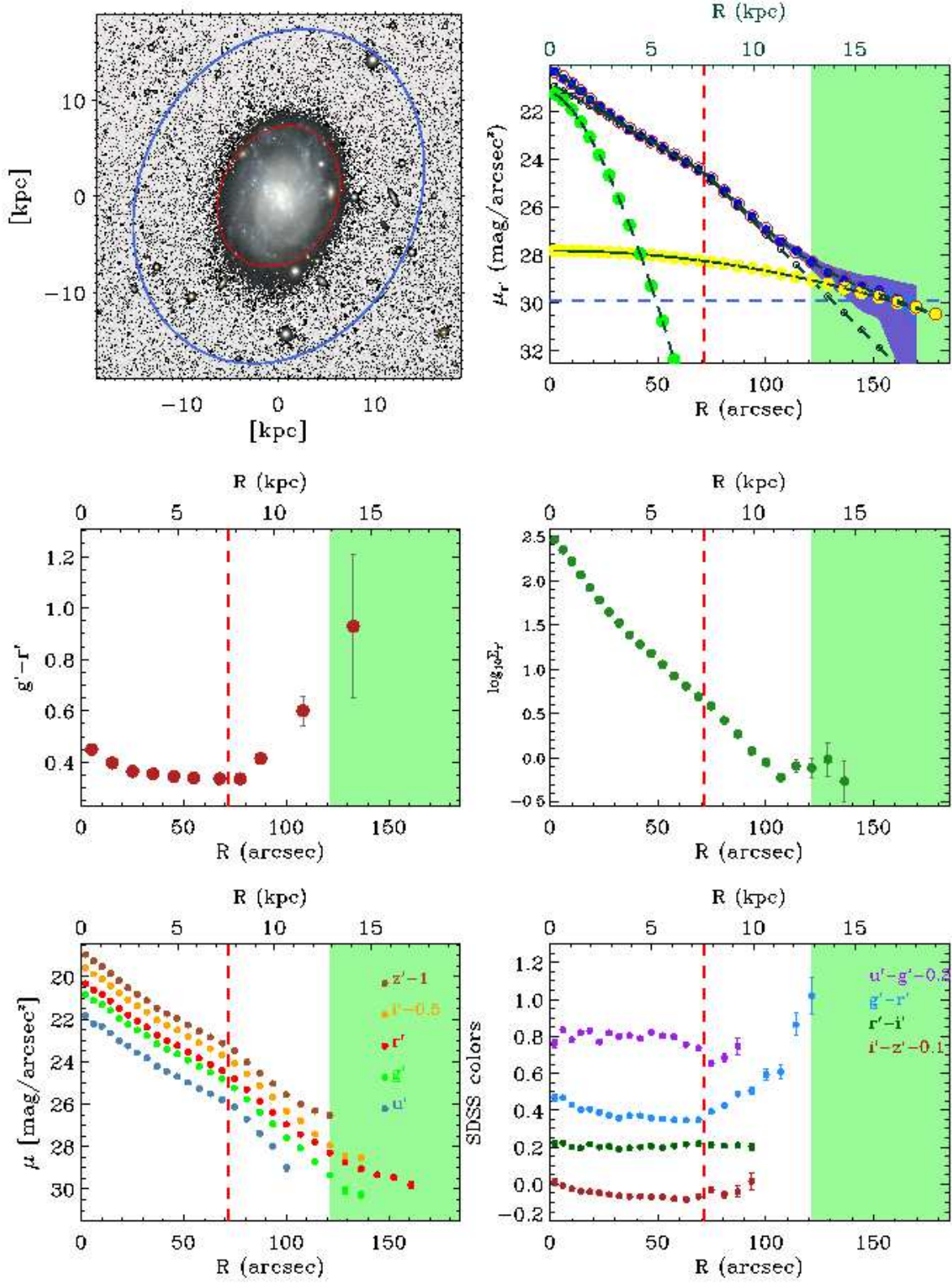


Figure 9. NGC 0941: It is a moderately inclined SABc type galaxy. It is within a small group of galaxies, though seems remarkably isolated and the disk shows no signs of interaction. It has a small bar that generates the pseudobulge feature observed at $R \lesssim 30''$ (Kormendy, private communication). The break lies at ~ 70 arcseconds (~ 7.5 kpc), and is classified as Type II-CT.

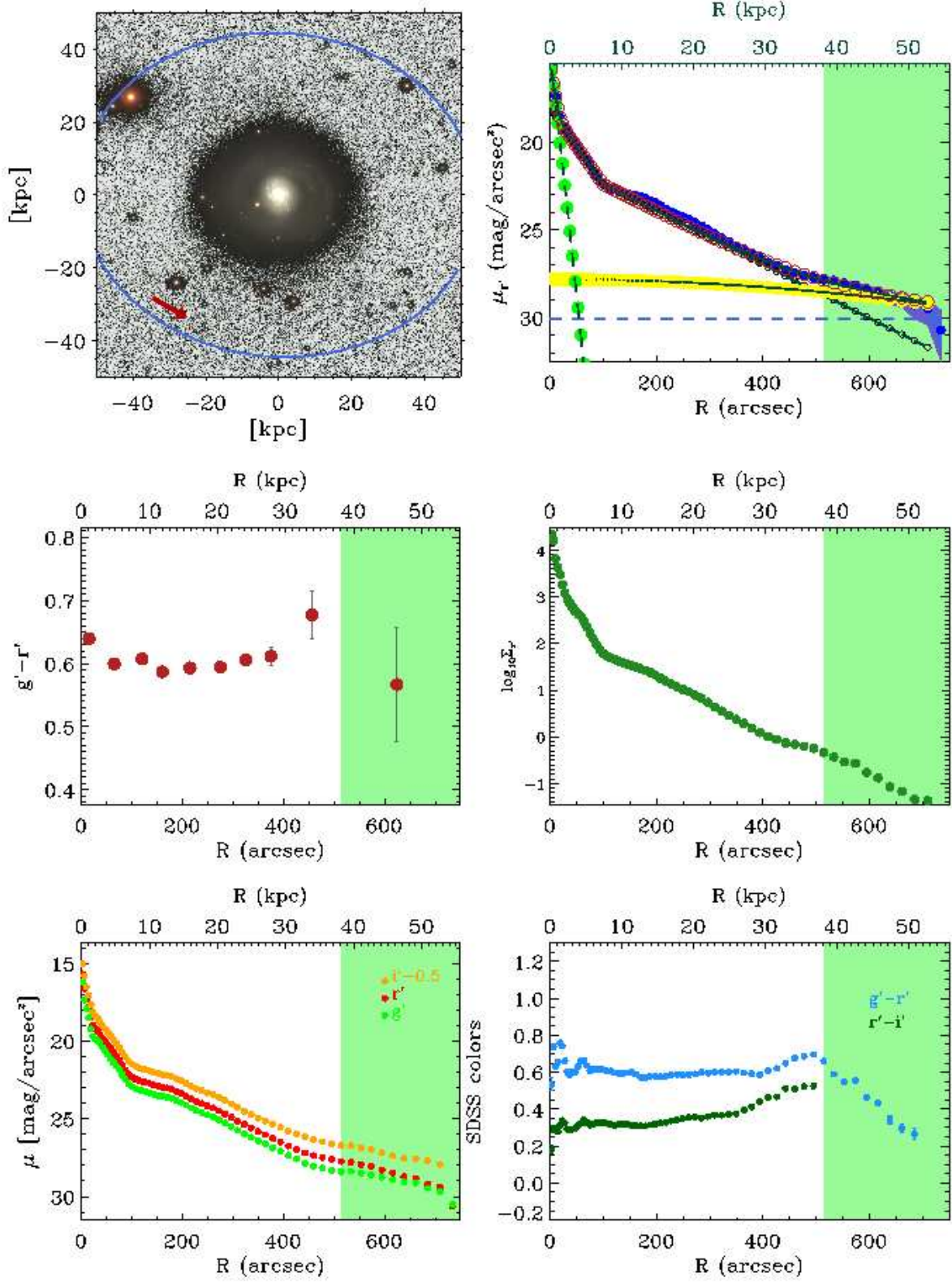


Figure 10. NGC 1068 or M77: This galaxy is a frequently studied, bright galaxy, with a Seyfert 2 class AGN (Khachikian & Weedman 1974) in its center. NGC 1068 appears to have a complex inner structure. According to Erwin (2004) this is a double-barred galaxy with a small inner bar ($R < 20''$) embedded within an oval distortion (extending out to $R \lesssim 200''$; Schinnerer et al. 2000) also remarked by Kormendy & Kennicutt (2004). We consider the structure outside $R \gtrsim 200''$ as the genuine disk of the galaxy. This galaxy is basically analogous to NGC 4736 (M94) (see also e.g. Trujillo et al. 2009) showing a strikingly similar overall morphology. Considering all these morphological features, this galaxy, based on its r' -band surface brightness profile, has been classified as Type I. The extended outer disk shows signs of interaction and misalignment, probably a result of recent bombardment. We report here the discovery of a low surface brightness ($\mu_{r'} \sim 27$ mag arcsec⁻²) satellite found at the coordinates $\alpha = 02 : 43 : 00$ $\delta = -00 : 09 : 01$. This object is indicated with a red arrow.

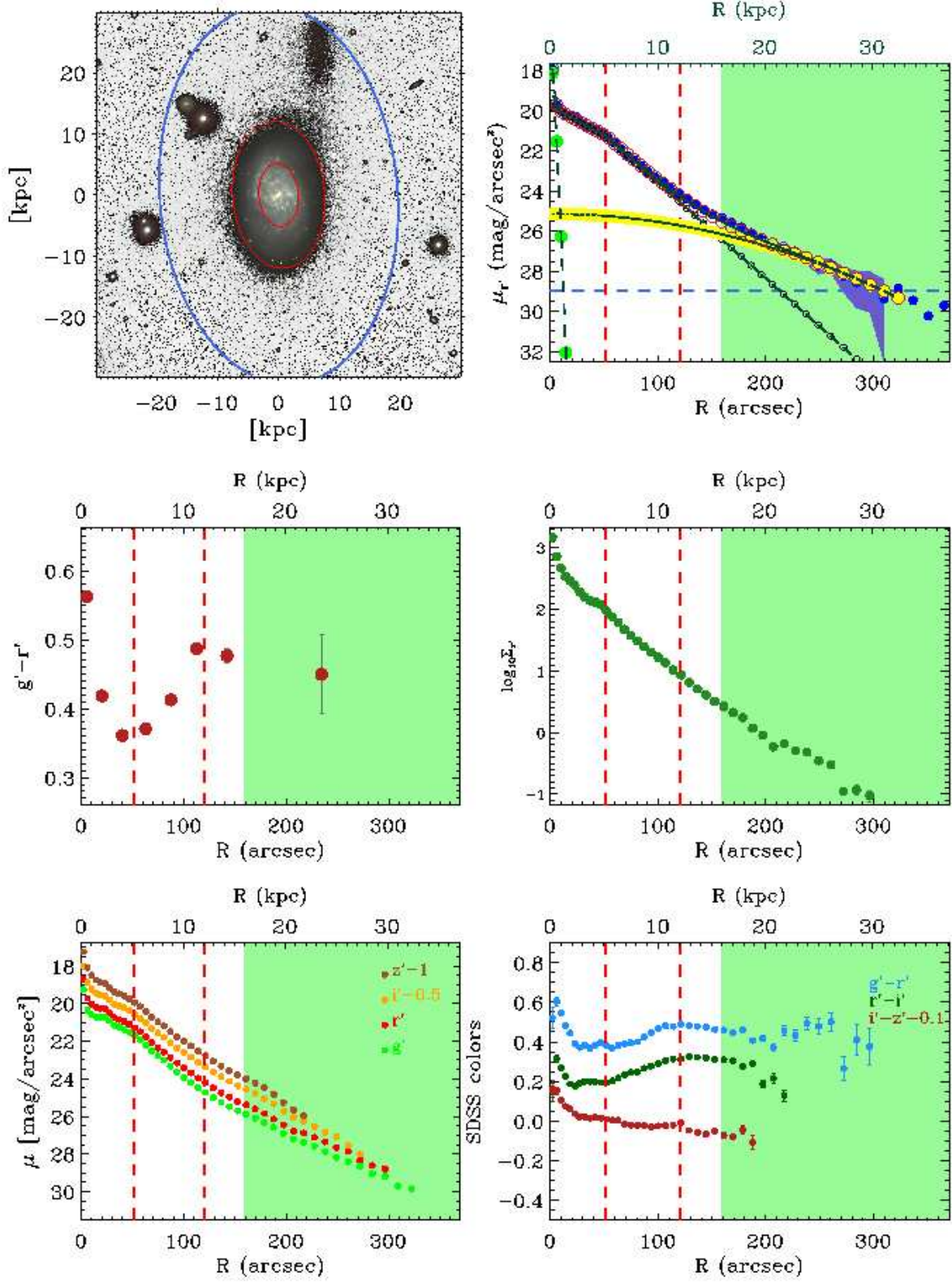


Figure 11. NGC 1087: It is a bright, SABc type galaxy with a misaligned outer disk that shows signs of an ongoing interaction on the North side of the galaxy. NGC 1087 is classified as Type II*+III: the apparent Type II break is due to the central star forming region in the inner disk, meanwhile the bright Type III like feature starting at $R \sim 120''$ appears because of the presence of an unusually bright stellar halo (due to this, this galaxy previously was classified as Type III in PT06).

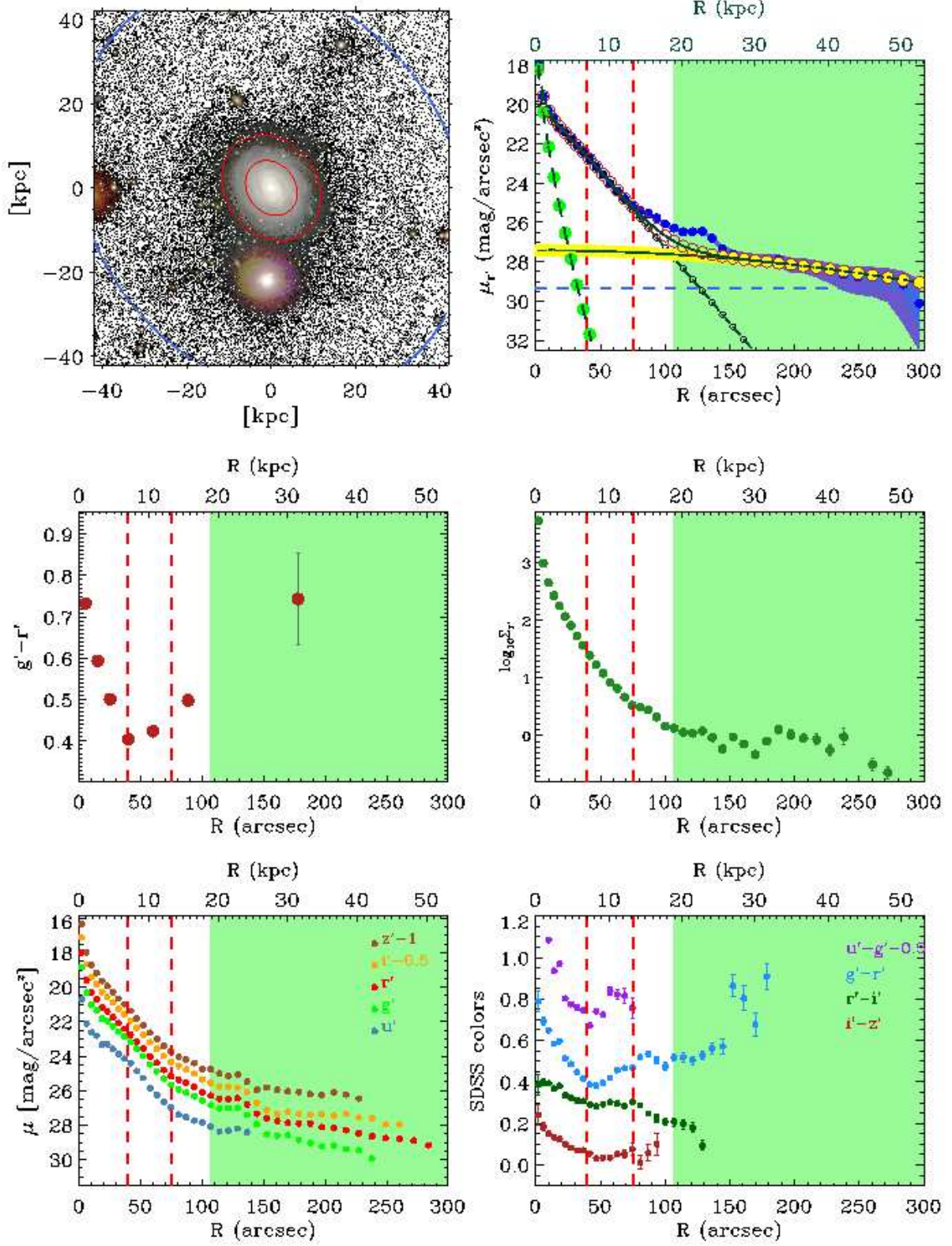


Figure 12. NGC 7716: One of the most interesting galaxies of our sample. This galaxy shows no peculiarities on its DR7 image, but its *Stripe82* counterpart reveals the presence of a misaligned outer disk and stellar streams. We cannot identify the progenitor satellites of these streams from the images (curiously enough the object that looks like a bright satellite to the North of NGC 7716 is just a background galaxy). Unfortunately, the nearby bright star obscures a part of the stellar stream. The other, jet-like feature is possibly another stream projected along our light-of-sight. NGC 7716 is classified as Type II*+III, following the previous classification scheme. The Type III feature, however, is clearly linked to the presence of the bright stellar stream and is part of the stellar halo.

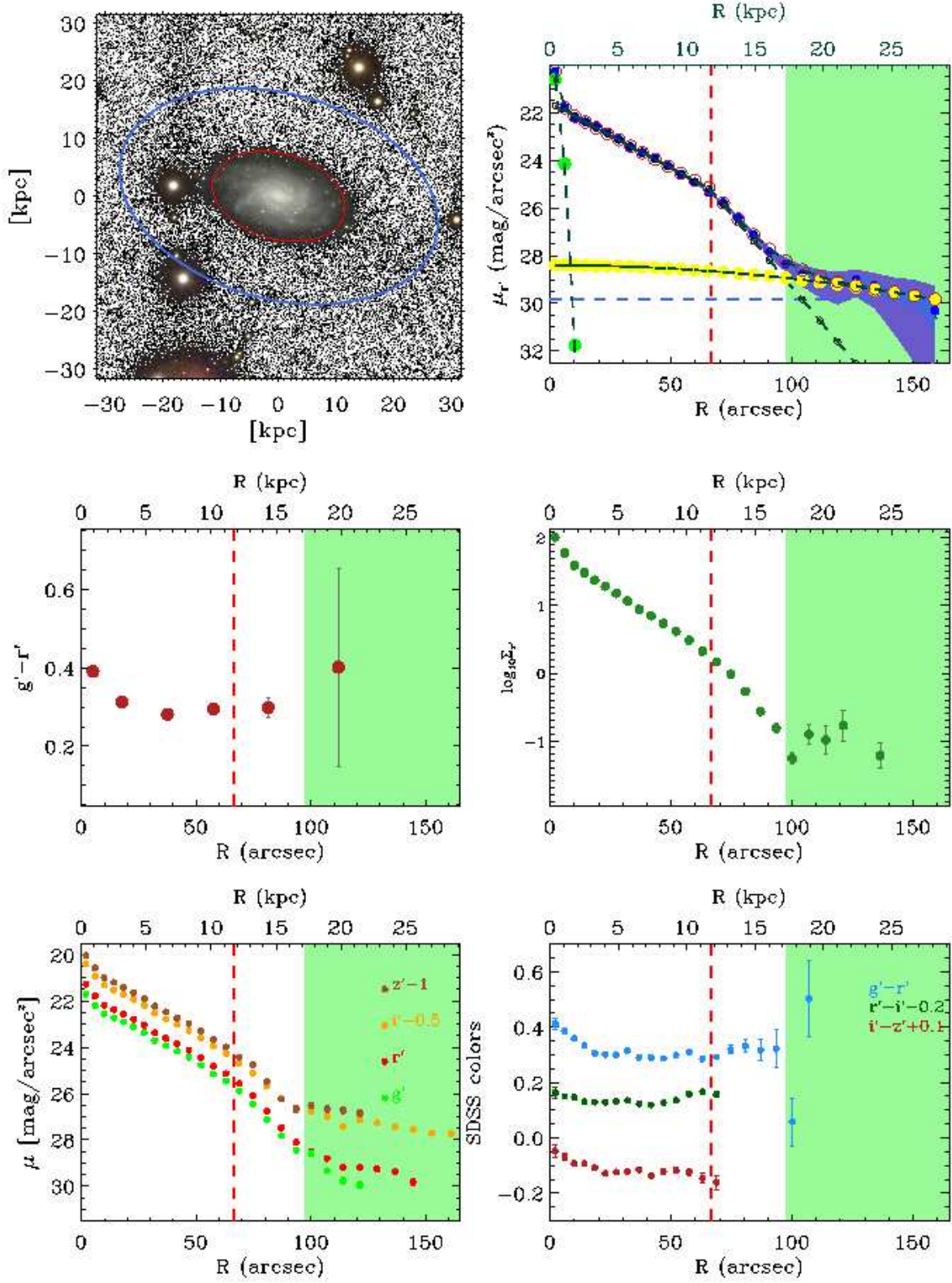


Figure 13. UGC 02081: Faint, moderately inclined SABc spiral. The bar is not obvious from the image, nor from the profile. It has a faint break at $\mu_r \sim 25$ mag arcsec⁻² and is classified as Type II-CT.

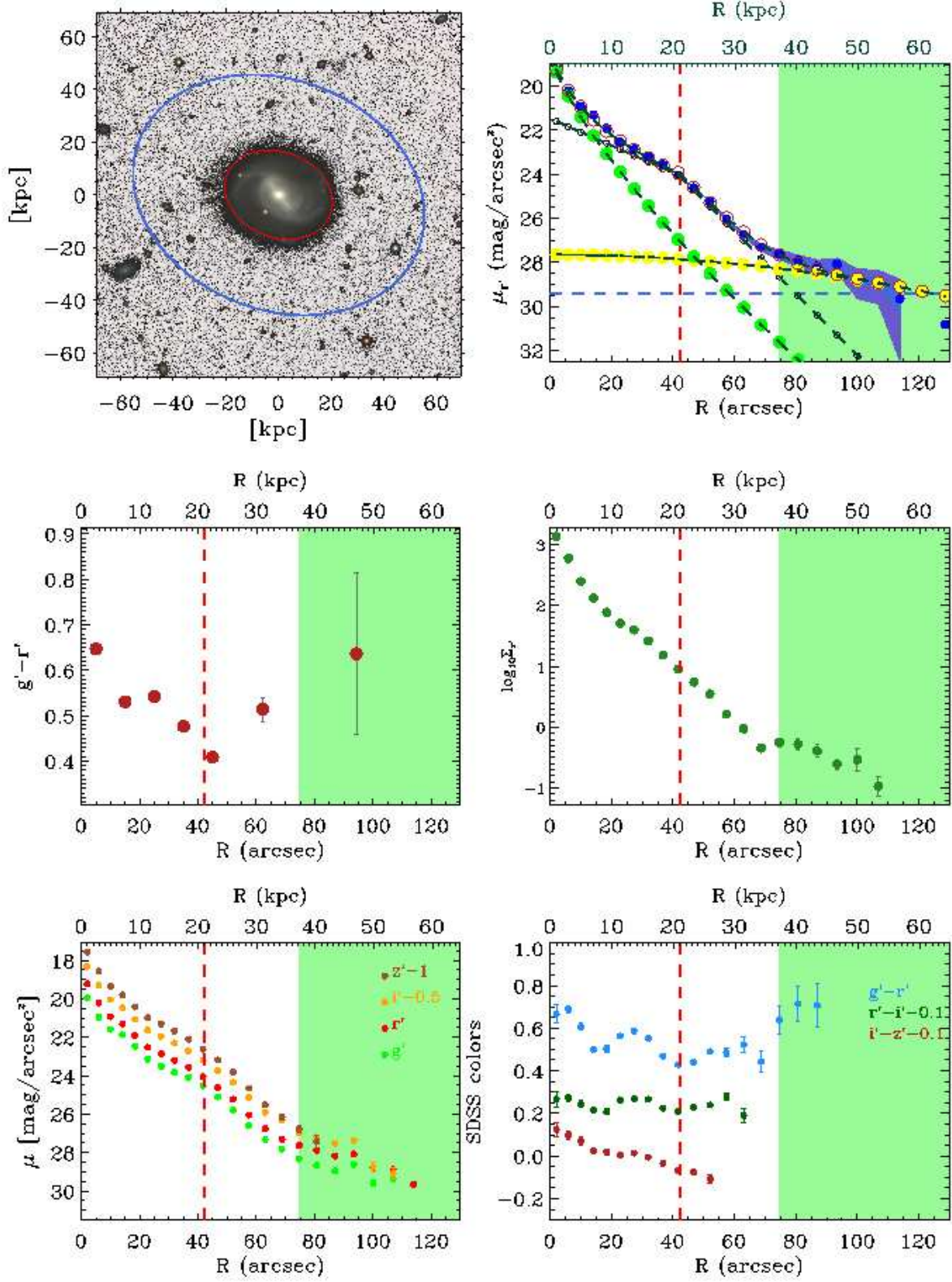


Figure 14. UGC 02311: Bright galaxy with a strong bar and with an apparent star forming resonance ring. The break position coincides with the position of the ring, therefore this galaxy is classified as Type II-ORL.

B. SURFACE BRIGHTNESS PROFILES

In this section we publish the surface brightness profiles of our galaxies obtained from the *Stripe82* imaging in the 5 SDSS bands. For some of our galaxies, the u'-band and z'-band detector problems prevented us to create reliable mosaics. In these cases (NGC 1068, NGC 1087, UGC 02081, and UGC 02311 in the u'-band and NGC 1068 in the z'-band) we did not use the u'- and z'-band stacks for further analysis.

Table 6
Surface brightness profiles of NGC0450

Radius	$\mu_{u'}$	$\mu_{g'}$	$\mu_{r'}$	$\mu_{i'}$	$\mu_{z'}$
[arcsec]	[mag arcsec ⁻²]	[mag arcsec ⁻²]	[mag arcsec ⁻²]	[mag arcsec ⁻²]	[mag arcsec ⁻²]
2.0	21.44 ± 0.02	20.26 ± 0.02	19.80 ± 0.01	19.55 ± 0.01	19.32 ± 0.01
5.9	22.08 ± 0.02	20.90 ± 0.01	20.40 ± 0.01	20.15 ± 0.01	19.92 ± 0.01
10.0	22.67 ± 0.01	21.43 ± 0.01	20.92 ± 0.01	20.66 ± 0.01	20.45 ± 0.01
14.1	22.90 ± 0.01	21.77 ± 0.01	21.26 ± 0.01	21.03 ± 0.01	20.83 ± 0.01
18.4	23.12 ± 0.01	22.03 ± 0.00	21.56 ± 0.00	21.32 ± 0.00	21.13 ± 0.00
22.8	23.23 ± 0.01	22.20 ± 0.00	21.78 ± 0.00	21.55 ± 0.00	21.38 ± 0.00
27.3	23.40 ± 0.01	22.39 ± 0.01	21.98 ± 0.01	21.77 ± 0.00	21.61 ± 0.01
31.9	23.62 ± 0.01	22.60 ± 0.01	22.18 ± 0.01	21.98 ± 0.00	21.82 ± 0.01
36.7	23.66 ± 0.01	22.66 ± 0.01	22.27 ± 0.01	22.09 ± 0.01	21.93 ± 0.01
41.7	23.76 ± 0.01	22.73 ± 0.01	22.36 ± 0.01	22.19 ± 0.01	22.04 ± 0.01
46.8	23.84 ± 0.01	22.81 ± 0.00	22.47 ± 0.00	22.31 ± 0.00	22.16 ± 0.01
52.0	23.99 ± 0.01	22.96 ± 0.00	22.63 ± 0.00	22.47 ± 0.00	22.33 ± 0.00
57.4	24.22 ± 0.01	23.17 ± 0.00	22.84 ± 0.00	22.67 ± 0.00	22.54 ± 0.00
63.0	24.34 ± 0.01	23.36 ± 0.00	23.03 ± 0.00	22.87 ± 0.00	22.74 ± 0.00
68.7	24.41 ± 0.01	23.51 ± 0.00	23.22 ± 0.00	23.07 ± 0.00	22.94 ± 0.00
74.6	24.47 ± 0.01	23.61 ± 0.00	23.34 ± 0.00	23.22 ± 0.00	23.09 ± 0.01
80.7	24.76 ± 0.01	23.85 ± 0.00	23.56 ± 0.00	23.44 ± 0.00	23.32 ± 0.01
87.0	25.16 ± 0.01	24.19 ± 0.01	23.88 ± 0.00	23.76 ± 0.01	23.66 ± 0.01
93.4	25.59 ± 0.02	24.56 ± 0.01	24.20 ± 0.01	24.06 ± 0.01	23.93 ± 0.01
100.1	25.95 ± 0.02	24.94 ± 0.01	24.58 ± 0.01	24.44 ± 0.01	24.32 ± 0.01
106.9	26.56 ± 0.03	25.36 ± 0.01	24.98 ± 0.01	24.86 ± 0.01	24.72 ± 0.01
113.9	27.46 ± 0.05	25.88 ± 0.01	25.42 ± 0.01	25.33 ± 0.01	25.17 ± 0.02
121.2	28.70 ± 0.14	26.42 ± 0.01	25.90 ± 0.01	25.86 ± 0.01	25.64 ± 0.03
128.7	...	26.94 ± 0.01	26.33 ± 0.01	26.28 ± 0.02	26.15 ± 0.04
136.4	...	27.38 ± 0.02	26.72 ± 0.01	26.82 ± 0.02	26.57 ± 0.05
144.3	...	27.78 ± 0.03	27.02 ± 0.02	27.27 ± 0.03	26.89 ± 0.07
152.5	...	28.16 ± 0.04	27.22 ± 0.02	27.47 ± 0.04	27.43 ± 0.11
160.9	...	28.51 ± 0.04	27.53 ± 0.02	27.99 ± 0.06	...
169.6	...	28.86 ± 0.06	27.79 ± 0.03	28.30 ± 0.07	...
178.5	...	29.20 ± 0.08	27.92 ± 0.03
187.7	28.20 ± 0.04
197.2	28.41 ± 0.04
206.9	28.57 ± 0.05
217.0	28.76 ± 0.06
227.3	28.81 ± 0.06
238.0	29.10 ± 0.08

Table 7
Surface brightness profiles of NGC0941

Radius	$\mu_{u'}$	$\mu_{g'}$	$\mu_{r'}$	$\mu_{i'}$	$\mu_{z'}$
[arcsec]	[mag arcsec ⁻²]	[mag arcsec ⁻²]	[mag arcsec ⁻²]	[mag arcsec ⁻²]	[mag arcsec ⁻²]
2.0	21.84 ± 0.02	20.83 ± 0.02	20.33 ± 0.01	20.08 ± 0.01	19.95 ± 0.01
5.9	22.20 ± 0.01	21.12 ± 0.01	20.62 ± 0.01	20.37 ± 0.00	20.26 ± 0.00
10.0	22.33 ± 0.01	21.30 ± 0.01	20.84 ± 0.01	20.61 ± 0.00	20.51 ± 0.01
14.1	22.65 ± 0.01	21.59 ± 0.01	21.15 ± 0.01	20.93 ± 0.01	20.85 ± 0.01
18.4	23.03 ± 0.01	21.95 ± 0.01	21.51 ± 0.01	21.27 ± 0.00	21.19 ± 0.00
22.8	23.25 ± 0.01	22.24 ± 0.00	21.81 ± 0.00	21.59 ± 0.00	21.51 ± 0.00
27.3	23.58 ± 0.01	22.51 ± 0.00	22.10 ± 0.00	21.88 ± 0.00	21.81 ± 0.00
31.9	23.82 ± 0.01	22.77 ± 0.00	22.38 ± 0.00	22.17 ± 0.00	22.11 ± 0.00
36.7	24.21 ± 0.01	23.16 ± 0.00	22.75 ± 0.00	22.53 ± 0.00	22.48 ± 0.00
41.7	24.45 ± 0.01	23.42 ± 0.00	23.01 ± 0.00	22.79 ± 0.00	22.73 ± 0.00
46.8	24.70 ± 0.01	23.63 ± 0.00	23.24 ± 0.00	23.01 ± 0.00	22.96 ± 0.00
52.0	24.97 ± 0.01	23.92 ± 0.00	23.53 ± 0.00	23.31 ± 0.00	23.26 ± 0.01
57.4	25.27 ± 0.01	24.22 ± 0.00	23.84 ± 0.00	23.61 ± 0.00	23.57 ± 0.01
63.0	25.51 ± 0.01	24.51 ± 0.00	24.12 ± 0.00	23.89 ± 0.00	23.85 ± 0.01
68.7	25.79 ± 0.01	24.81 ± 0.00	24.42 ± 0.00	24.18 ± 0.00	24.13 ± 0.01
74.6	26.14 ± 0.02	25.24 ± 0.01	24.81 ± 0.01	24.57 ± 0.01	24.49 ± 0.01
80.7	26.70 ± 0.02	25.77 ± 0.01	25.31 ± 0.01	25.08 ± 0.01	25.01 ± 0.02
87.0	27.38 ± 0.04	26.38 ± 0.01	25.86 ± 0.01	25.63 ± 0.01	25.54 ± 0.03
93.4	27.99 ± 0.07	26.94 ± 0.01	26.39 ± 0.01	26.17 ± 0.02	26.03 ± 0.04
100.1	28.99 ± 0.16	27.58 ± 0.02	26.95 ± 0.02	26.81 ± 0.03	26.56 ± 0.06
106.9	...	28.07 ± 0.03	27.43 ± 0.02	27.28 ± 0.03	27.00 ± 0.09
113.9	...	28.70 ± 0.05	27.80 ± 0.03	27.91 ± 0.06	27.31 ± 0.11
121.2	...	29.35 ± 0.09	28.29 ± 0.05	28.44 ± 0.09	...
128.7	28.75 ± 0.07	28.93 ± 0.13	...
136.4	29.05 ± 0.09
144.3	29.33 ± 0.10

Table 8
Surface brightness profiles of NGC1068

Radius	$\mu_{g'}$	$\mu_{r'}$	$\mu_{i'}$
[arcsec]	[mag arcsec ⁻²]	[mag arcsec ⁻²]	[mag arcsec ⁻²]
2.0	16.35 ± 0.03	15.78 ± 0.02	15.58 ± 0.02
5.9	17.49 ± 0.01	16.71 ± 0.01	16.40 ± 0.01
10.0	18.06 ± 0.01	17.39 ± 0.01	17.08 ± 0.01
14.1	18.61 ± 0.01	17.92 ± 0.01	17.62 ± 0.01
18.4	19.36 ± 0.01	18.56 ± 0.01	18.23 ± 0.01
22.8	19.84 ± 0.01	19.06 ± 0.01	18.70 ± 0.00
27.3	20.00 ± 0.00	19.30 ± 0.00	18.96 ± 0.00
31.9	20.08 ± 0.00	19.44 ± 0.00	19.13 ± 0.00
36.7	20.27 ± 0.00	19.65 ± 0.00	19.34 ± 0.00
41.7	20.53 ± 0.00	19.90 ± 0.00	19.58 ± 0.00
46.8	20.75 ± 0.00	20.11 ± 0.00	19.79 ± 0.00
52.0	21.00 ± 0.00	20.33 ± 0.00	20.00 ± 0.00
57.4	21.26 ± 0.00	20.57 ± 0.00	20.22 ± 0.00
63.0	21.51 ± 0.00	20.81 ± 0.00	20.45 ± 0.00
68.7	21.72 ± 0.00	21.05 ± 0.00	20.70 ± 0.00
74.6	21.94 ± 0.00	21.30 ± 0.00	20.97 ± 0.00
80.7	22.28 ± 0.00	21.63 ± 0.00	21.29 ± 0.00
87.0	22.60 ± 0.00	21.95 ± 0.00	21.60 ± 0.00
93.4	22.86 ± 0.00	22.21 ± 0.00	21.86 ± 0.00
100.1	23.06 ± 0.00	22.41 ± 0.00	22.06 ± 0.00
106.9	23.18 ± 0.00	22.54 ± 0.00	22.20 ± 0.00
113.9	23.27 ± 0.00	22.62 ± 0.00	22.28 ± 0.00
121.2	23.32 ± 0.00	22.68 ± 0.00	22.35 ± 0.00
128.7	23.39 ± 0.00	22.76 ± 0.00	22.42 ± 0.00
136.4	23.48 ± 0.00	22.85 ± 0.00	22.51 ± 0.00
144.3	23.57 ± 0.00	22.94 ± 0.00	22.60 ± 0.00
152.5	23.65 ± 0.00	23.01 ± 0.00	22.68 ± 0.00
160.9	23.69 ± 0.00	23.06 ± 0.00	22.73 ± 0.00
169.6	23.72 ± 0.00	23.11 ± 0.00	22.78 ± 0.00
178.5	23.80 ± 0.00	23.19 ± 0.00	22.86 ± 0.00
187.7	23.94 ± 0.00	23.33 ± 0.00	22.99 ± 0.00
197.2	24.07 ± 0.00	23.46 ± 0.00	23.12 ± 0.00
206.9	24.24 ± 0.00	23.63 ± 0.00	23.29 ± 0.00
217.0	24.43 ± 0.00	23.81 ± 0.00	23.46 ± 0.00
227.3	24.60 ± 0.00	23.98 ± 0.00	23.62 ± 0.00
238.0	24.74 ± 0.00	24.12 ± 0.00	23.75 ± 0.00
249.0	24.88 ± 0.00	24.26 ± 0.00	23.89 ± 0.00
260.3	25.01 ± 0.00	24.39 ± 0.00	24.01 ± 0.00
271.9	25.20 ± 0.00	24.57 ± 0.00	24.19 ± 0.00
283.9	25.41 ± 0.00	24.77 ± 0.00	24.40 ± 0.00
296.3	25.62 ± 0.00	24.99 ± 0.00	24.60 ± 0.00
309.0	25.87 ± 0.00	25.23 ± 0.00	24.84 ± 0.00
322.1	26.09 ± 0.00	25.46 ± 0.00	25.07 ± 0.00
335.6	26.32 ± 0.00	25.68 ± 0.00	25.29 ± 0.00
349.5	26.55 ± 0.00	25.91 ± 0.00	25.51 ± 0.00
363.9	26.74 ± 0.00	26.11 ± 0.00	25.69 ± 0.00
378.6	26.99 ± 0.00	26.36 ± 0.00	25.93 ± 0.00
393.8	27.20 ± 0.00	26.58 ± 0.00	26.12 ± 0.00
409.5	27.49 ± 0.00	26.84 ± 0.00	26.36 ± 0.00
425.6	27.69 ± 0.01	27.04 ± 0.00	26.55 ± 0.00
442.2	27.97 ± 0.01	27.29 ± 0.01	26.75 ± 0.01
459.3	28.17 ± 0.01	27.46 ± 0.01	26.93 ± 0.01
476.9	28.31 ± 0.01	27.59 ± 0.01	27.04 ± 0.01
495.1	28.44 ± 0.01	27.71 ± 0.01	27.17 ± 0.01
513.8	28.53 ± 0.01	27.83 ± 0.01	27.28 ± 0.01
533.0	28.50 ± 0.01	27.88 ± 0.01	27.30 ± 0.01
552.9	28.62 ± 0.01	28.04 ± 0.01	27.44 ± 0.01
573.3	28.74 ± 0.01	28.15 ± 0.01	27.52 ± 0.01
594.3	28.89 ± 0.01	28.39 ± 0.01	27.73 ± 0.01
616.0	29.05 ± 0.01	28.58 ± 0.01	27.94 ± 0.01
638.3	29.18 ± 0.01	28.81 ± 0.02	28.12 ± 0.01
661.3	29.25 ± 0.01	28.92 ± 0.02	28.15 ± 0.01
685.0	29.59 ± 0.02	29.29 ± 0.02	28.27 ± 0.02
709.4	29.82 ± 0.02	29.47 ± 0.03	28.50 ± 0.02
734.5	30.64 ± 0.05	30.71 ± 0.08	...

Table 9
Surface brightness profiles of NGC1087

Radius	$\mu_{g'}$	$\mu_{r'}$	$\mu_{i'}$	$\mu_{z'}$
[arcsec]	[mag arcsec ⁻²]	[mag arcsec ⁻²]	[mag arcsec ⁻²]	[mag arcsec ⁻²]
2.0	19.25 ± 0.04	18.70 ± 0.04	18.53 ± 0.03	18.25 ± 0.03
5.9	20.35 ± 0.01	19.71 ± 0.01	19.37 ± 0.01	19.10 ± 0.01
10.0	20.60 ± 0.01	20.02 ± 0.01	19.73 ± 0.01	19.50 ± 0.01
14.1	20.70 ± 0.01	20.18 ± 0.01	19.94 ± 0.00	19.74 ± 0.01
18.4	20.74 ± 0.00	20.26 ± 0.00	20.05 ± 0.00	19.87 ± 0.00
22.8	20.71 ± 0.00	20.28 ± 0.00	20.08 ± 0.00	19.92 ± 0.00
27.3	20.91 ± 0.01	20.51 ± 0.00	20.29 ± 0.00	20.15 ± 0.00
31.9	21.16 ± 0.00	20.74 ± 0.00	20.52 ± 0.00	20.38 ± 0.00
36.7	21.24 ± 0.00	20.84 ± 0.00	20.62 ± 0.00	20.48 ± 0.00
41.7	21.37 ± 0.00	20.95 ± 0.00	20.73 ± 0.00	20.59 ± 0.00
46.8	21.52 ± 0.00	21.09 ± 0.00	20.87 ± 0.00	20.74 ± 0.00
52.0	21.71 ± 0.00	21.29 ± 0.00	21.08 ± 0.00	20.94 ± 0.00
57.4	21.91 ± 0.00	21.50 ± 0.00	21.28 ± 0.00	21.15 ± 0.00
63.0	22.20 ± 0.00	21.78 ± 0.00	21.54 ± 0.00	21.42 ± 0.00
68.7	22.50 ± 0.00	22.08 ± 0.00	21.82 ± 0.00	21.72 ± 0.00
74.6	22.78 ± 0.00	22.34 ± 0.00	22.08 ± 0.00	21.98 ± 0.00
80.7	23.01 ± 0.00	22.57 ± 0.00	22.30 ± 0.00	22.20 ± 0.00
87.0	23.33 ± 0.00	22.87 ± 0.00	22.58 ± 0.00	22.48 ± 0.00
93.4	23.64 ± 0.00	23.16 ± 0.00	22.86 ± 0.00	22.76 ± 0.00
100.1	23.93 ± 0.00	23.42 ± 0.00	23.11 ± 0.00	23.01 ± 0.00
106.9	24.20 ± 0.00	23.68 ± 0.00	23.35 ± 0.00	23.26 ± 0.00
113.9	24.48 ± 0.00	23.97 ± 0.00	23.63 ± 0.00	23.53 ± 0.00
121.2	24.73 ± 0.00	24.20 ± 0.00	23.87 ± 0.00	23.75 ± 0.01
128.7	25.01 ± 0.00	24.49 ± 0.00	24.14 ± 0.00	24.07 ± 0.01
136.4	25.25 ± 0.00	24.74 ± 0.00	24.39 ± 0.00	24.33 ± 0.01
144.3	25.48 ± 0.00	24.97 ± 0.00	24.63 ± 0.00	24.57 ± 0.01
152.5	25.70 ± 0.00	25.20 ± 0.00	24.86 ± 0.00	24.80 ± 0.01
160.9	25.88 ± 0.00	25.39 ± 0.00	25.05 ± 0.00	25.00 ± 0.01
169.6	26.09 ± 0.00	25.60 ± 0.00	25.28 ± 0.01	25.23 ± 0.02
178.5	26.35 ± 0.01	25.85 ± 0.01	25.55 ± 0.01	25.47 ± 0.02
187.7	26.58 ± 0.01	26.14 ± 0.01	25.83 ± 0.01	25.82 ± 0.03
197.2	26.90 ± 0.01	26.45 ± 0.01	26.24 ± 0.01	26.26 ± 0.05
206.9	27.20 ± 0.01	26.79 ± 0.02	26.55 ± 0.02	26.65 ± 0.07
217.0	27.38 ± 0.02	26.89 ± 0.02	26.74 ± 0.02	26.98 ± 0.09
227.3	27.58 ± 0.02	27.11 ± 0.02	27.05 ± 0.03	27.26 ± 0.11
238.0	27.88 ± 0.02	27.35 ± 0.02	27.35 ± 0.04	27.98 ± 0.20
249.0	28.17 ± 0.03	27.66 ± 0.03	27.57 ± 0.04	28.08 ± 0.20
260.3	28.40 ± 0.03	27.87 ± 0.03	28.05 ± 0.06	...
271.9	28.63 ± 0.04	28.33 ± 0.05	28.51 ± 0.08	...
283.9	29.05 ± 0.05	28.61 ± 0.06	29.04 ± 0.13	...
296.3	29.19 ± 0.06	28.78 ± 0.07	30.47 ± 0.42	...
309.0	29.70 ± 0.10	29.38 ± 0.12
322.1	29.85 ± 0.11	29.04 ± 0.09
335.6	30.44 ± 0.17	29.33 ± 0.11
349.5	...	31.36 ± 0.55

Table 10
Surface brightness profiles of NGC7716

Radius	$\mu_{u'}$	$\mu_{g'}$	$\mu_{r'}$	$\mu_{i'}$	$\mu_{z'}$
[arcsec]	[mag arcsec ⁻²]	[mag arcsec ⁻²]	[mag arcsec ⁻²]	[mag arcsec ⁻²]	[mag arcsec ⁻²]
2.0	20.69 ± 0.03	18.84 ± 0.03	18.01 ± 0.04	17.60 ± 0.04	17.34 ± 0.04
5.9	22.11 ± 0.01	20.32 ± 0.01	19.60 ± 0.01	19.17 ± 0.01	18.97 ± 0.01
10.0	22.63 ± 0.00	21.00 ± 0.00	20.32 ± 0.00	19.90 ± 0.00	19.73 ± 0.00
14.1	22.81 ± 0.01	21.33 ± 0.01	20.71 ± 0.01	20.32 ± 0.00	20.16 ± 0.00
18.4	23.33 ± 0.01	21.82 ± 0.01	21.18 ± 0.00	20.78 ± 0.00	20.64 ± 0.00
22.8	23.31 ± 0.01	21.96 ± 0.00	21.42 ± 0.00	21.06 ± 0.00	20.94 ± 0.00
27.3	23.59 ± 0.01	22.26 ± 0.00	21.74 ± 0.00	21.40 ± 0.00	21.30 ± 0.00
31.9	23.87 ± 0.01	22.57 ± 0.00	22.09 ± 0.00	21.75 ± 0.00	21.67 ± 0.00
36.7	24.15 ± 0.01	22.86 ± 0.00	22.41 ± 0.00	22.08 ± 0.00	21.99 ± 0.00
41.7	24.41 ± 0.01	23.19 ± 0.00	22.77 ± 0.00	22.45 ± 0.00	22.38 ± 0.00
46.8	24.87 ± 0.01	23.58 ± 0.00	23.16 ± 0.00	22.86 ± 0.00	22.80 ± 0.01
52.0	25.26 ± 0.01	23.99 ± 0.00	23.56 ± 0.00	23.25 ± 0.00	23.20 ± 0.01
57.4	25.86 ± 0.02	24.48 ± 0.00	24.02 ± 0.00	23.70 ± 0.00	23.64 ± 0.01
63.0	26.25 ± 0.02	24.88 ± 0.00	24.39 ± 0.00	24.07 ± 0.00	24.00 ± 0.01
68.7	26.66 ± 0.04	25.30 ± 0.01	24.80 ± 0.01	24.49 ± 0.01	24.42 ± 0.02
74.6	26.97 ± 0.05	25.67 ± 0.01	25.16 ± 0.01	24.83 ± 0.01	24.74 ± 0.03
80.7	27.38 ± 0.06	25.93 ± 0.01	25.38 ± 0.01	25.07 ± 0.01	25.04 ± 0.03
87.0	27.55 ± 0.08	26.12 ± 0.01	25.55 ± 0.01	25.28 ± 0.01	25.20 ± 0.04
93.4	27.73 ± 0.09	26.31 ± 0.01	25.77 ± 0.01	25.52 ± 0.01	25.40 ± 0.05
100.1	27.84 ± 0.09	26.59 ± 0.01	26.08 ± 0.01	25.85 ± 0.02	25.73 ± 0.06
106.9	28.09 ± 0.10	26.85 ± 0.01	26.29 ± 0.01	26.06 ± 0.02	25.77 ± 0.05
113.9	28.36 ± 0.12	27.03 ± 0.02	26.47 ± 0.01	26.26 ± 0.02	26.02 ± 0.06
121.2	28.33 ± 0.11	27.01 ± 0.01	26.47 ± 0.01	26.27 ± 0.02	26.16 ± 0.07
128.7	28.20 ± 0.10	27.01 ± 0.01	26.44 ± 0.01	26.33 ± 0.02	26.06 ± 0.06
136.4	28.41 ± 0.11	27.40 ± 0.02	26.81 ± 0.02	26.58 ± 0.02	26.47 ± 0.08
144.3	29.24 ± 0.20	27.94 ± 0.03	27.34 ± 0.02	27.20 ± 0.03	26.95 ± 0.11
152.5	29.11 ± 0.18	28.53 ± 0.04	27.63 ± 0.03	27.61 ± 0.04	26.82 ± 0.09
160.9	29.27 ± 0.20	28.60 ± 0.05	27.76 ± 0.03	27.86 ± 0.06	26.95 ± 0.10
169.6	29.49 ± 0.22	28.57 ± 0.04	27.86 ± 0.03	27.72 ± 0.05	27.05 ± 0.11
178.5	...	28.85 ± 0.05	27.91 ± 0.03	27.86 ± 0.05	27.07 ± 0.10
187.7	...	29.03 ± 0.06	27.91 ± 0.03	27.90 ± 0.05	27.21 ± 0.11
197.2	...	29.22 ± 0.07	28.11 ± 0.04	27.87 ± 0.05	27.25 ± 0.11
206.9	...	29.21 ± 0.06	28.14 ± 0.04	27.95 ± 0.05	27.09 ± 0.10
217.0	...	29.39 ± 0.07	28.29 ± 0.04	27.84 ± 0.04	27.23 ± 0.10
227.3	...	29.47 ± 0.08	28.46 ± 0.04	28.06 ± 0.05	27.46 ± 0.13
238.0	...	29.94 ± 0.12	28.66 ± 0.06	28.10 ± 0.05	27.56 ± 0.14
249.0	...	30.41 ± 0.18	28.75 ± 0.06	28.46 ± 0.07	27.42 ± 0.12
260.3	...	29.68 ± 0.09	28.79 ± 0.06	28.46 ± 0.07	27.77 ± 0.16
271.9	...	29.69 ± 0.09	28.90 ± 0.06	28.55 ± 0.07	27.57 ± 0.13
283.9	...	30.13 ± 0.12	29.16 ± 0.08	28.98 ± 0.10	27.88 ± 0.17
296.3	...	32.10 ± 0.56	30.14 ± 0.16	30.59 ± 0.36	27.98 ± 0.17
309.0	29.99 ± 0.14	...	28.93 ± 0.36
322.1	29.90 ± 0.12
335.6	30.17 ± 0.15
349.5	31.03 ± 0.30

Table 11
Surface brightness profiles of UGC02081

Radius	$\mu_{g'}$	$\mu_{r'}$	$\mu_{i'}$	$\mu_{z'}$
[arcsec]	[mag arcsec ⁻²]	[mag arcsec ⁻²]	[mag arcsec ⁻²]	[mag arcsec ⁻²]
2.0	21.71 ± 0.01	21.27 ± 0.01	20.89 ± 0.02	21.02 ± 0.02
5.9	22.21 ± 0.01	21.79 ± 0.01	21.42 ± 0.01	21.58 ± 0.01
10.0	22.56 ± 0.00	22.18 ± 0.00	21.81 ± 0.00	21.99 ± 0.00
14.1	22.73 ± 0.00	22.37 ± 0.00	22.02 ± 0.00	22.19 ± 0.00
18.4	22.90 ± 0.00	22.57 ± 0.00	22.22 ± 0.00	22.42 ± 0.00
22.8	23.11 ± 0.00	22.78 ± 0.00	22.44 ± 0.00	22.65 ± 0.00
27.3	23.37 ± 0.00	23.04 ± 0.00	22.69 ± 0.00	22.90 ± 0.00
31.9	23.71 ± 0.00	23.37 ± 0.00	23.02 ± 0.00	23.22 ± 0.01
36.7	23.93 ± 0.00	23.61 ± 0.00	23.27 ± 0.00	23.47 ± 0.01
41.7	24.17 ± 0.00	23.85 ± 0.00	23.51 ± 0.00	23.73 ± 0.01
46.8	24.43 ± 0.00	24.12 ± 0.00	23.77 ± 0.00	23.98 ± 0.01
52.0	24.77 ± 0.00	24.45 ± 0.00	24.10 ± 0.00	24.30 ± 0.01
57.4	25.15 ± 0.00	24.81 ± 0.00	24.43 ± 0.00	24.64 ± 0.01
63.0	25.45 ± 0.00	25.14 ± 0.00	24.76 ± 0.01	24.99 ± 0.02
68.7	25.88 ± 0.01	25.56 ± 0.01	25.19 ± 0.01	25.44 ± 0.02
74.6	26.44 ± 0.01	26.09 ± 0.01	25.63 ± 0.01	25.76 ± 0.03
80.7	27.12 ± 0.02	26.76 ± 0.02	26.20 ± 0.02	26.48 ± 0.06
87.0	27.81 ± 0.03	27.47 ± 0.03	26.70 ± 0.02	27.24 ± 0.11
93.4	28.45 ± 0.05	28.10 ± 0.05	27.13 ± 0.04	27.66 ± 0.16
100.1	28.58 ± 0.05	28.49 ± 0.07	27.26 ± 0.04	27.51 ± 0.14
106.9	29.34 ± 0.10	28.80 ± 0.09	27.49 ± 0.05	27.67 ± 0.16
113.9	29.78 ± 0.14	29.19 ± 0.12	27.92 ± 0.07	27.71 ± 0.16
121.2	29.94 ± 0.16	29.17 ± 0.11	27.65 ± 0.05	27.85 ± 0.18
128.7	30.59 ± 0.25	29.26 ± 0.10	27.77 ± 0.05	28.21 ± 0.21
136.4	...	29.37 ± 0.12	27.92 ± 0.06	...
144.3	...	29.82 ± 0.16	28.05 ± 0.06	...
152.5	...	29.81 ± 0.15	28.20 ± 0.07	...
160.9	...	30.60 ± 0.29	28.24 ± 0.07	...
169.6	28.47 ± 0.08	...
178.5	28.66 ± 0.10	...
187.7	29.00 ± 0.13	...
197.2	29.15 ± 0.14	...
206.9	29.67 ± 0.21	...

Table 12
Surface brightness profiles of UGC02311

Radius	$\mu_{g'}$	$\mu_{r'}$	$\mu_{i'}$	$\mu_{z'}$
[arcsec]	[mag arcsec ⁻²]	[mag arcsec ⁻²]	[mag arcsec ⁻²]	[mag arcsec ⁻²]
2.0	19.95 ± 0.03	19.23 ± 0.03	18.83 ± 0.03	18.57 ± 0.02
5.9	20.95 ± 0.01	20.21 ± 0.01	19.80 ± 0.01	19.57 ± 0.01
10.0	21.59 ± 0.01	20.92 ± 0.01	20.55 ± 0.01	20.34 ± 0.01
14.1	21.87 ± 0.01	21.32 ± 0.01	20.96 ± 0.01	20.81 ± 0.01
18.4	22.47 ± 0.01	21.91 ± 0.01	21.57 ± 0.01	21.42 ± 0.01
22.8	23.15 ± 0.01	22.53 ± 0.01	22.13 ± 0.01	21.99 ± 0.01
27.3	23.51 ± 0.01	22.86 ± 0.01	22.46 ± 0.01	22.31 ± 0.01
31.9	23.82 ± 0.00	23.21 ± 0.00	22.81 ± 0.00	22.68 ± 0.01
36.7	24.10 ± 0.00	23.57 ± 0.00	23.21 ± 0.00	23.11 ± 0.01
41.7	24.53 ± 0.01	24.04 ± 0.01	23.70 ± 0.01	23.63 ± 0.01
46.8	25.10 ± 0.01	24.61 ± 0.01	24.24 ± 0.01	24.18 ± 0.01
52.0	25.78 ± 0.01	25.23 ± 0.01	24.86 ± 0.01	24.83 ± 0.02
57.4	26.59 ± 0.02	26.05 ± 0.01	25.63 ± 0.01	25.66 ± 0.04
63.0	27.32 ± 0.03	26.74 ± 0.02	26.42 ± 0.03	26.52 ± 0.09
68.7	27.82 ± 0.04	27.32 ± 0.03	26.81 ± 0.04	27.16 ± 0.14
74.6	28.32 ± 0.05	27.63 ± 0.04	27.50 ± 0.06	27.77 ± 0.20
80.7	28.67 ± 0.07	27.90 ± 0.04	27.71 ± 0.07	...
87.0	28.95 ± 0.08	28.19 ± 0.05	28.02 ± 0.08	...
93.4	28.62 ± 0.06	28.08 ± 0.05	27.87 ± 0.07	...
100.1	29.62 ± 0.14	28.76 ± 0.08	29.25 ± 0.22	...
106.9	29.37 ± 0.11	28.87 ± 0.09
113.9	29.89 ± 0.16	29.65 ± 0.16